Ore Geology Reviews 122 (2020) 103481

Contents lists available at ScienceDirect

Ore Geology Reviews

journal homepage: www.elsevier.com/locate/oregeorev

Formation of the Cretaceous skarn Cu–Au deposits of the southern Gangdese belt, Tibet: Case studies of the Kelu and Sangbujiala deposits

Wenting Huang[a], Huaying Liang[a,*], Jian Zhang[c], Xilian Chen[d], Lin Shuping[g], Yinqiao Zou[h], Long Ren[a], Jing Wu[e], Lipeng Zhang[b,f]

[a] Key Laboratory of Mineralogy and Metallogeny, Guangzhou Institute of Geochemistry, Chinese Academy of Sciences, Guangzhou 510640, China
[b] Laboratory for Marine Geology, Qingdao National Laboratory for Marine Science and Technology, Qingdao 266061, China
[c] Key Laboratory of Environment Change and Resources Use in Beibu Gulf, Ministry of Education, Nanning Normal University, Nanning 530004, China
[d] State Key Laboratory of Nuclear Resources and Environment, East China University of Technology, Nanchang 330013, China
[e] College of Resources, Environment and Materials, Guangxi University, Nanning 530004, China
[f] Center of Deep Sea Research, Institute of Oceanology, Center for Ocean Mega-Science, Chinese Academy of Sciences, Qingdao 266071, China
[g] Chongqing Key Laboratory of Geological Survey of Land Quality, Chongqing 404100, China
[h] Country Garden Center, Foshan 528312, China

ARTICLE INFO

Keywords:
Gangdese
Cu–Au mineralization
Cretaceous
Adakitic rocks
Neo-Tethyan subduction

ABSTRACT

Mesozoic subduction of Neo-Tethyan oceanic crust caused magmatism that formed numerous Jurassic and Cretaceous intrusions within the southern Gangdese belt of Tibet. These intrusions are associated with the formation of giant Jurassic Xiongcun porphyry Cu deposits, but the prospectivity of other Cretaceous intrusions in this area remains unclear. This study presents new molybdenite Re–Os ages for the Kelu and Sangbujiala Cu–Au skarn deposits within the southern Gangdese belt as well as new geochemical, zircon U–Pb geochronological, and Sr–Nd–Hf isotopic data for the intrusions associated with these deposits. These new data indicate that (1) the Kelu deposit formed at ca. 92 Ma, coeval with emplacement of the diorite and biotite granodiorite intrusions (ca. 92–90 Ma) in this area, and (2) the Sangbujiala deposit formed at ca. 95 Ma, contemporaneous with emplacement of the mineralized biotite granodiorite (ca. 95–92 Ma) in this area. These data suggest that the skarn Cu–Au mineralization in this area formed as a result of Cretaceous magmatism in the southern Gangdese belt. The intrusions associated with the Kelu and Sangbujiala deposits have adakitic affinities with low contents of Y and heavy rare-earth elements and high Sr/Y ratios (22.4–123). These intrusions also have more primitive Sr–Nd isotopic compositions ($\varepsilon_{Nd}(t)$ = 3.99–4.81, $(^{87}Sr/^{86}Sr)_i$ = 0.7040–0.7044), lower $\varepsilon_{Hf}(t)$ values (8.0–13.18), and higher zircon Eu_N/Eu^* values (mean of 0.50) than those of contemporaneous but barren adakitic intrusions in this region. This suggests that the mineralization-related intrusions were oxidized and formed from magmas that were generated predominantly by partial melting of subducted Neo-Tethyan slab material without any significant crustal contamination or assimilation of sedimentary material. However, these intrusions contain elevated Th, Ni, and Cr contents, and have high $Mg^{\#}$ ratios (43.4–56.9), suggesting that they formed from magmas that interacted with metasomatized mantle wedge peridotite material. Combining our new data with the results of previous research suggests that the southern Gangdese belt records two stages of Cu–Au mineralization related to Neo-Tethyan subduction. The first stage generated the large Xiongcun porphyry Cu–Au deposit and was associated with normal subduction during the Jurassic, whereas the second stage was associated with the formation of the Kelu and Sangbujiala skarn deposits during Cretaceous slab rollback.

1. Introduction

The southern Gangdese belt records the northward-directed Mesozoic subduction of Neo-Tethyan oceanic crust and the Cenozoic collision of India with Eurasia (Yin and Harrison, 2000). The latter event was associated with the formation of numerous Miocene (ca. 18–10 Ma) porphyry Cu–(Mo) deposits (Hou et al., 2004, 2009, 2015b; Huang et al., 2013; Li et al., 2011; Qu et al., 2004; Wang et al., 2014a,b, 2017) that delineate a porphyry deposit belt within the southern Gangdese region. Neo-Tethyan subduction also generated numerous Cretaceous and lesser amounts of Jurassic intrusions in this region (Chung et al., 2005; Ji et al., 2009a; Ma et al., 2013a, 2013b, 2013c;

* Corresponding author.
E-mail address: lianghy@gig.ac.cn (H. Liang).

https://doi.org/10.1016/j.oregeorev.2020.103481
Received 30 June 2019; Received in revised form 15 February 2020; Accepted 17 March 2020
Available online 19 March 2020
0169-1368/

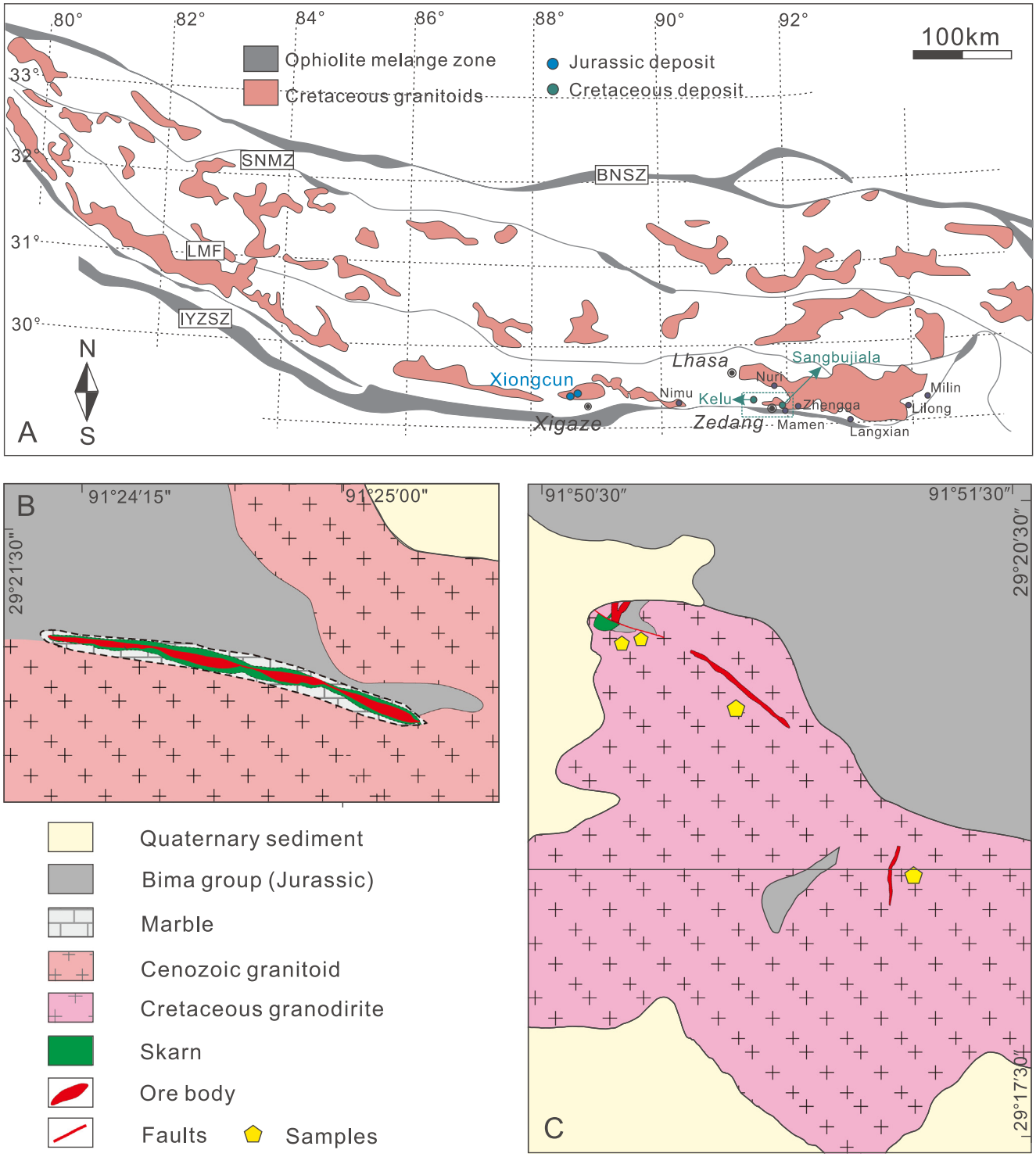

Fig. 1. (A) Simplified geological map showing the distribution of Cretaceous intrusions in the Gangdese belt of southern Tibet (modified after Zhu et al., 2011). (B) Geological map of the Kelu skarn Cu–Au deposit. (C) Geological map of the Sangbujiala skarn Cu–Au deposit.

Sun et al., 2019; Wen et al., 2008b; Zhu et al., 2011; Zou et al., 2017). These include an Early–Middle Jurassic belt of highly oxidized magmatism that is associated with the large Xiongcun porphyry Cu–Au deposit as well as a number of other mineralized occurrences (Chen et al., 2019a; Tafti et al., 2009; Wang et al., 2017; Xie et al., 2018; Zou et al., 2015, 2017). This ggests that the Jurassic subduction event in this region caused widespread magmatism that led to the formation of associated porphyry Cu mineralization. However, little is known about mineralization associated with the Cretaceous magmatism in this area. For example, Jiang et al. (2012) reported that the Kelu skarn Cu–Au deposit was associated with Cretaceous felsic igneous rocks in the southern Gangdese belt. However, the timing of formation of this deposit and the geochemistry of the associated intrusions remain unknown, hindering our understanding of the processes that formed the Cretaceous mineralization-related magmas within the southern Gangdese belt.

This study presents new molybdenite Re–Os ages for the Kelu and Sangbujiala skarn-type Cu–Au deposits of the southern Gangdese belt as

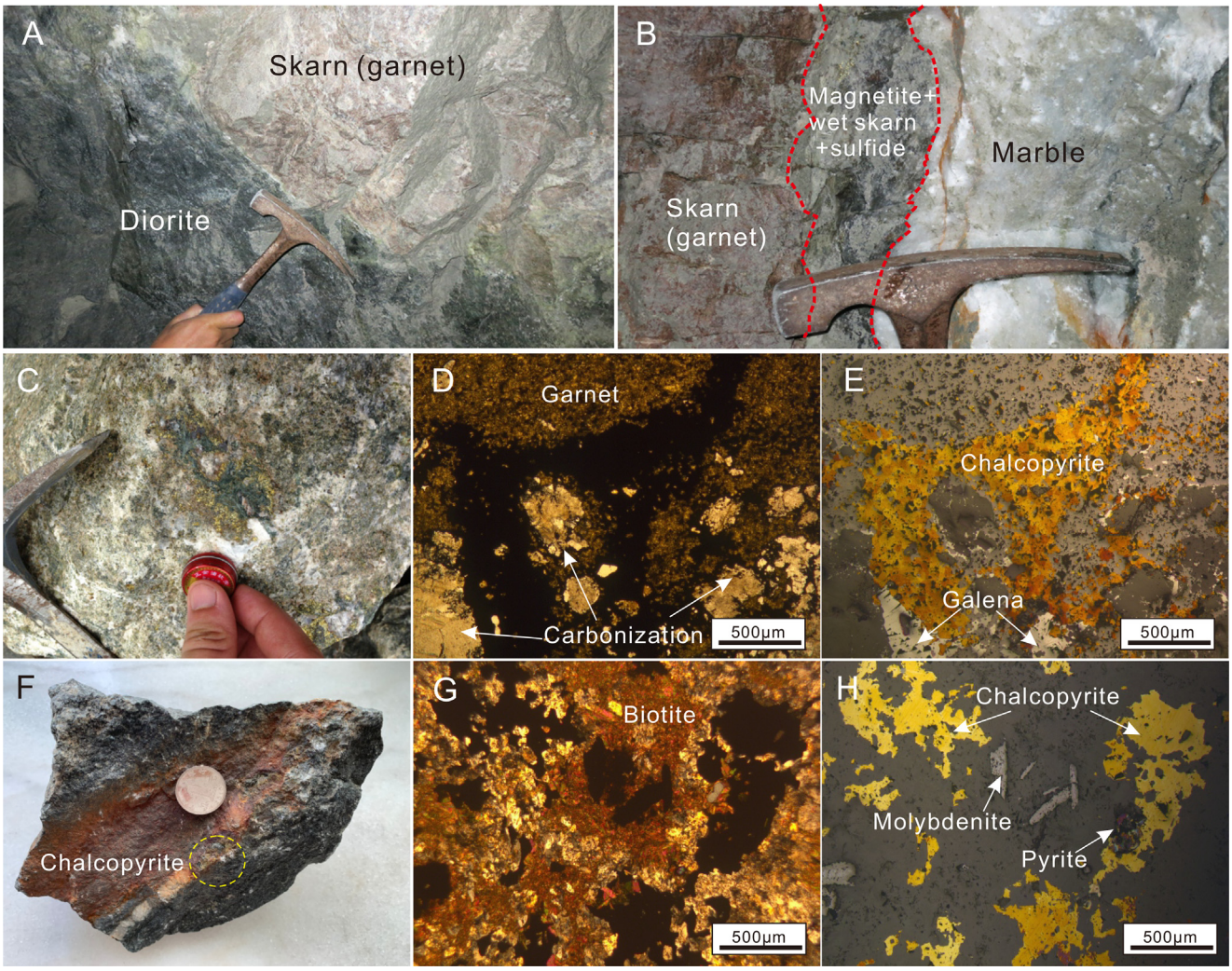

Fig. 2. Representative photographs and photomicrographs of samples from the Kelu (A–E) and Sangbujiala (F–H) Cu–Au deposits. (A) Contact between diorite and skarn. (B) Skarn, sulfides, and marble within the outer contact zone. (C) Representative ore hand specimen. (D–E) Photomicrographs taken under transmitted (D) and reflected (E) light showing garnet-dominated skarn and Cu mineralization. (F) Representative hand specimen showing a Cu-rich mineralized vein. (G–H) Photomicrographs taken under transmitted (G) and reflected (H) light showing biotite-dominated potassic alteration and Cu mineralization.

well as geochemical, zircon U–Pb geochronological, and Sr–Nd–Hf isotopic data for the intrusions associated with these deposits. These new data provide insights into mineralization associated with subduction of Neo-Tethyan oceanic crust as well as the timing of mineralization within the entire Gangdese belt.

2. Regional geology

The Tibetan plateau is divided from north to south into the Songpan–Ganze, Yidun, Qiangtang, Lhasa, and Tethyan Himalayan terranes, which are separated by the Jinshajing, Bangong–Nujiang, and Yarlung–Tsangpo sutures, respectively (Yin and Harrison, 2000). The Lhasa terrane is bounded by the Yarlung–Tsangpo suture to the south and the Bangong–Nuijiang suture to the north and has a southern margin that contains a series of Mesozoic–Cenozoic magmatic rocks that define the Gangdese magmatic belt. The magmatic rocks within this belt formed as a result of Jurassic–Cretaceous subduction of Neo-Tethyan oceanic crust and the subsequent collision of India with Eurasia during the early Tertiary (Chung et al., 2009; Yin and Harrison, 2000). The sedimentary rocks within the Gangdese belt include Mesozoic volcanic–sedimentary rocks of the Bima and Sangri formations and Paleogene–Eocene volcanic–sedimentary rocks of the Linzizong Group, as well as small amounts of Permian limestone and Carboniferous sedimentary units (Kang et al., 2014). The intrusions in this region are dominated by Cenozoic granitoids and Cretaceous–Jurassic arc-type granites, as well as relatively minor volumes of Triassic–Jurassic granitic intrusions (Chen et al., 2019a,b; Chu et al., 2006; Hou et al., 2015b; Ji et al., 2009b; Zhu et al., 2017; Zou et al., 2017).

The exposed Jurassic intrusions within the Gangdese belt define an E–W-oriented ~150-km-long belt located between Xietongmen and Nanmling. The majority of these plutons are small (< 2 km^2) and are dominated by granodiorite, diorite, granite, quartz monzonite, tonalite, and gabbro phases. Early–Middle Jurassic (ca. 185–165 Ma) porphyritic granodiorite intrusions within the Xietongmen district are genetically associated with the giant Xiongcun porphyry Cu–Au deposit (Tang et al., 2015; Zou et al., 2015; Chen et al., 2019a).

Cretaceous mafic–felsic magmatic rocks are widely distributed along the southern margin of the Gangdese belt. These units formed as a result of a Cretaceous (ca. 100–80 Ma) magmatic 'flare-up' within the southern Gangdese belt (e.g., Wen et al., 2008a, 2008b; Zhu et al., 2009). A large number of these intrusions (e.g., those within the Milin, Langxian, Linnong, Mamen, and Nuri areas) have adakitic affinities (Wen et al., 2008a; Zhu et al., 2009; Zhang et al., 2010; Ma et al., 2013a; Zheng et al., 2014; Xu et al., 2015), although comparatively few are associated with mineralization, with one key exception being the skarn-type Kelu Cu–Au deposit (Jiang et al., 2012).

3. Deposit geology

The Kelu–Sangbujiala area is located within the southern edge of the Gangdese belt (Fig. 1) and contains Jurassic volcanic–sedimentary, Cretaceous sedimentary, and Paleocene volcanic–sedimentary units. The Jurassic volcanic–sedimentary rocks are dominated by units containing tuffaceous andesite, rhyolite, quartz sandstone, and tuffs intercalated with sandstone and limestone, all of which form part of the Jurassic Bima Group (BGMRXAR, 1993). Cretaceous sedimentary rocks are dominated by slate, coarse-grained quartz sandstone, shale, mudstone, and marlstone units (BGMRXAR, 1993). The Paleocene volcanic–sedimentary rocks consist of Cenozoic andesite, dacite, volcanic breccia, and tuff units (BGMRXAR, 1993). The area also contains voluminous granitoid intrusions that were emplaced predominantly during the Cenozoic, with comparatively few intrusions forming during the Mesozoic (Jiang et al., 2012).

The Kelu skarn Cu–Au deposit is located in the western part of the Kelu–Sangbujiala region (Fig. 1) and contains reserves of 17.77 t of Au at grades of 2.4–4.2 g/t and 144.4 thousand tons of Cu at an average grade of 3.2%. The area around the deposit contains units of the Jurassic Bima Group as well as a Cenozoic biotite granite intrusion (Fig. 1B). The Cu–Au mineralization is hosted within an E–W-striking skarn vein that cross-cuts Birma Group limestone units. Underground observations indicate that the skarn in this area formed along a contact between marble units and concealed diorite and biotite granodiorite dikes (Fig. 2A). The diorite contains plagioclase (40 vol%–45 vol%), amphibole (35 vol%–40 vol%), K-feldspar (10 vol%–15 vol%), quartz (~5 vol%), and minor amounts of biotite (< vol.5%; Fig. 3A) whereas the biotite granodiorite contains plagioclase (40 vol%–45 vol%), quartz (~vol.20%), K-feldspar (15 vol%–20 vol%), biotite (10 vol%–15 vol%), and minor amounts of amphibole (< 5 vol%; Fig. 3B). Both diorite and biotite granodiorite units are spatially associated with skarn development and Cu–Au mineralization. These dikes are associated with alteration zones that change from proximal anhydrous skarn (e.g., garnet and magnetite) to hydrous skarn (e.g., epidote and actinolite), sulfide, and distal marble assemblages (Fig. 2B), suggesting that the dikes are genetically related to the skarn mineralization. The ore mineralogy of the deposit is dominated by chalcopyrite, bornite, tetrahedrite, pyrite, magnetite, sphalerite, galena, and minor amounts of molybdenite, all of which are hosted by a garnet, actinolite, epidote, calcite, quartz, and chlorite gangue (Fig. 2C–E).

The small Sangbujiala skarn-type Cu–(Au) deposit is located within the eastern part of the Kelu–Sangbujiala area (Fig. 1) and contains low-grade gold mineralization. This area contains the Chemen granodiorite, units of the Bima Group, and Quaternary sediments (BGMRXAR, 1993). The Chemen intrusion crops out over an area of ~20 km^2 and is dominated by a biotite granodiorite phase that contains plagioclase (40 vol%–45 vol%), quartz (20 vol%–25 vol%), K-feldspar (~15 vol%), biotite (~15 vol%), and minor amounts of amphibole (< 5 vol%; Fig. 3C), with accessory zircon, apatite, and titanite. The mineralization in this area is hosted by a skarn located between the Chemen biotite granodiorite and Bima Group limestones in the northwestern part of the area. Some mineralization is present as veins within the Chemen intrusion (Fig. 2F; Internal Report of Mining Company, 2014). This mineralization is associated with skarn and carbonate alteration along the contact between the intrusion and the limestone as well as proximal silicification and potassic, chlorite, and epidote alteration located near the vein-hosted mineralization (Fig. 2G). The main ore minerals are chalcopyrite, bornite, magnetite, and pyrite, all of which are hosted by a garnet, quartz, actinolite, calcite, biotite, chlorite, epidote, and sericite gangue assemblage (Fig. 2F–H).

4. Samples and analytical techniques

4.1. Zircon trace-element and U–Pb analyses

A single biotite granodiorite sample (14SN-1-3) from the Kelu deposit and two Chemen diorite granodiorite samples (SN18-3 and 14CM-3) from the Sangbujiala deposit (Sangbujiala biotite granodiorite hereafter) were analyzed during this study. Prior to analysis, zircons were separated by conventional standard density and magnetic techniques from ~1 kg rock samples before > 100 individual zircons were handpicked and mounted in an epoxy resin disc. The discs were then polished and imaged using cathodoluminescence (CL) prior to analysis.

Zircons were analyzed at the State Key Laboratory of Isotope Geochemistry (SKLIG) Guangzhou Institute of Geochemistry, Chinese Academy of Science (GIGCAS), Guangzhou, China. Single-zircon trace-element analysis and U–Pb dating was undertaken using inductively coupled plasma–mass spectrometry (ICP–MS) employing an Agilent 7500a quadrupole instrument and multi-collector (MC)–ICP–MS employing a Neptune instrument, both of which were coupled with a 193 nm excimer ArF laser ablation (LA) system. Analyses used round spots with a diameter of 25 μm, an output energy of ~80 mJ, and a repetition rate of 8 Hz (Tu et al., 2011). External calibration was undertaken using NIST SRM 610 glass (Pearce et al., 1997) and TEMORA zircon (Black et al., 2003) standards. The off-line inspection and integration of background and analytical signals, time drift corrections, and quantitative calibrations were all undertaken using the ICPMSDataCal software package (Liu et al., 2010), and concordia diagram construction and weighted mean age calculations were undertaken using the Isoplot/Ex_ver3 software package (Ludwig, 2003). Data with observed-error/expected-error ratios of > 2 or that had < 90% concordance between $^{207}Pb/^{235}U$ (or $^{208}Pb/^{232}Th$) and $^{206}Pb/^{238}U$ were discarded. Cumulative probability plots were used to identify lead inheritance and/or loss. Uncertainties on single age determinations are reported as 1σ values in Table 1 with weighted mean $^{206}Pb/^{238}U$ ages reported with 2σ uncertainties.

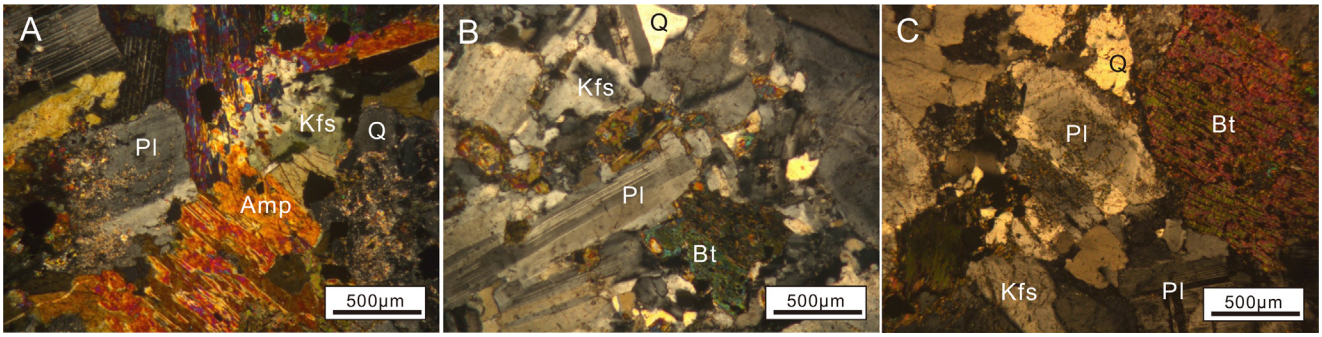

Fig. 3. Representative transmitted light photomicrographs showing the (A) diorite and (B) biotite granodiorite intrusions associated with the Kelu deposit and the (C) biotite granodiorite associated with the Sangbujiala deposit. Abbreviations: Amp = amphibole; Q = quartz; Bt = biotite; Kfs = K-feldspar; Pl = plagioclase.

Table 1
LA-ICP-MS zircon U-Pb dating results of intrusions in Kelu and Sangbujiala deposits.

Analysis	Pb	U	Th/U	Atomic Ratios								rho	Ages(Ma)						Concordance
	(ppm)			$^{206}Pb/^{238}U$	± 1σ	$^{207}Pb/^{235}U$	± 1σ	$^{207}Pb/^{206}Pb$	± 1σ	$^{208}Pb/^{232}Th$	± 1σ		$^{207}Pb/^{235}U$	± 1σ	$^{208}Pb/^{232}Th$	± 1σ	$^{206}Pb/^{238}U$	± 1σ	
14SN-1-3-1	18.50	846	1.63	0.01394	0.00025	0.08309	0.00328	0.04271	0.00184	0.00406	0.00014	0.45182	81.05	3.07	81.95	2.76	89.27	1.58	90%
14SN-1-3-2	6.12	313	0.66	0.01520	0.00037	0.11148	0.01057	0.05014	0.00421	0.00548	0.00033	0.25747	107.32	9.66	110.39	6.69	97.27	2.36	90%
14SN-1-3-3	18.22	759	1.80	0.01450	0.00022	0.09186	0.00352	0.04550	0.00186	0.00430	0.00013	0.38726	89.24	3.28	86.81	2.60	92.78	1.37	96%
14SN-1-3-4	13.48	645	1.42	0.01381	0.00022	0.08965	0.00343	0.04664	0.00185	0.00398	0.00013	0.41199	87.18	3.19	80.28	2.65	88.43	1.38	98%
14SN-1-3-5	15.34	736	1.27	0.01414	0.00020	0.08712	0.00345	0.04443	0.00186	0.00420	0.00015	0.36033	84.82	3.22	84.75	2.92	90.53	1.28	93%
14SN-1-3-6	18.44	779	1.76	0.01409	0.00022	0.10206	0.00476	0.05243	0.00248	0.00448	0.00015	0.33771	98.68	4.38	90.42	3.00	90.21	1.41	91%
14SN-1-3-7	7.59	377	0.90	0.01431	0.00031	0.09689	0.00604	0.04910	0.00298	0.00524	0.00021	0.34878	93.90	5.59	105.72	4.20	91.57	1.98	97%
14SN-1-3-8	7.44	333	1.11	0.01509	0.00037	0.10844	0.00667	0.05263	0.00320	0.00490	0.00019	0.39395	104.54	6.11	98.87	3.84	96.58	2.32	92%
14SN-1-3-9	15.14	667	1.86	0.01385	0.00021	0.09470	0.00357	0.04996	0.00206	0.00415	0.00012	0.40484	91.87	3.31	83.69	2.44	88.68	1.35	96%
14SN-1-3-10	10.77	487	1.47	0.01488	0.00029	0.10026	0.00529	0.04923	0.00263	0.00448	0.00015	0.36624	97.01	4.88	90.36	3.00	95.19	1.83	98%
14SN-1-3-11	10.36	257	1.12	0.02155	0.00086	0.64961	0.08535	0.19007	0.02118	0.01635	0.00175	0.30349	508.24	52.59	327.83	34.77	137.42	5.42	−15%
14SN-1-3-12	12.80	602	1.43	0.01421	0.00023	0.10042	0.00443	0.05133	0.00224	0.00432	0.00013	0.36503	97.17	4.08	87.03	2.54	90.99	1.45	93%
14SN-1-3-13	31.70	1349	1.92	0.01418	0.00019	0.09112	0.00298	0.04676	0.00160	0.00442	0.00012	0.40007	88.55	2.77	89.22	2.39	90.80	1.18	97%
14SN-1-3-14	20.25	867	1.79	0.01419	0.00018	0.10123	0.00425	0.05194	0.00220	0.00456	0.00015	0.30098	97.91	3.92	91.88	3.11	90.83	1.14	92%
14SN-1-3-15	8.06	378	1.37	0.01383	0.00028	0.09314	0.00490	0.04958	0.00283	0.00462	0.00016	0.38254	90.42	4.55	93.07	3.12	88.55	1.77	97%
14SN-1-3-16	12.31	458	1.58	0.01655	0.00055	0.41837	0.04382	0.17514	0.01581	0.00877	0.00085	0.31617	354.89	31.38	176.54	16.94	105.80	3.48	−9%
14SN-1-3-17	16.26	722	1.52	0.01491	0.00039	0.09412	0.00413	0.04576	0.00187	0.00461	0.00015	0.59548	91.34	3.83	92.92	3.03	95.42	2.47	95%
14SN-1-3-18	19.13	898	1.70	0.01318	0.00017	0.09257	0.00393	0.05061	0.00213	0.00417	0.00013	0.30519	89.89	3.65	84.21	2.67	84.40	1.09	93%
14SN-1-3-19	10.86	467	1.47	0.01452	0.00028	0.13643	0.00978	0.06677	0.00433	0.00507	0.00021	0.26969	129.86	8.74	102.17	4.20	92.95	1.79	66%
14SN-1-3-20	6.50	342	0.79	0.01444	0.00032	0.09539	0.00510	0.04847	0.00291	0.00448	0.00019	0.41331	92.51	4.73	90.42	3.79	92.43	2.03	99%
14SN-1-3-21	13.60	209	2.23	0.05881	0.01019	5.37926	1.21999	0.34840	0.04671	0.01344	0.00140	0.76417	1881.56	196.61	269.88	28.02	368.37	62.05	−35%
14SN-1-3-22	11.19	290	0.47	0.01861	0.00064	0.60571	0.06573	0.21642	0.01761	0.02638	0.00320	0.31535	480.85	41.59	526.22	62.93	118.84	4.03	−21%
14SN-1-3-23	9.56	423	1.32	0.01458	0.00033	0.17026	0.02004	0.08141	0.00909	0.00584	0.00035	0.19455	159.64	17.39	117.70	6.96	93.31	2.12	47%
14SN-1-3-24	18.82	188	0.98	0.03399	0.00189	2.30797	0.28049	0.46161	0.05517	0.04669	0.00475	0.45670	1214.74	86.30	922.26	91.72	215.45	11.76	−40%
14SN-1-3-25	9.43	426	1.65	0.01412	0.00032	0.09654	0.00488	0.04978	0.00264	0.00452	0.00021	0.45016	93.57	4.52	91.07	4.23	90.38	2.04	96%
14SN-1-3-26	10.75	574	0.64	0.01489	0.00030	0.10816	0.00478	0.05252	0.00229	0.00440	0.00021	0.45538	104.28	4.38	88.71	4.21	95.26	1.90	90%
14SN-1-3-27	12.32	445	0.38	0.01652	0.00060	0.38069	0.05748	0.15026	0.01463	0.01901	0.00177	0.24160	327.55	42.29	380.56	35.03	105.63	3.82	−3%
14SN-1-3-28	23.96	1046	1.88	0.01389	0.00023	0.09560	0.00481	0.04940	0.00221	0.00428	0.00014	0.33114	92.70	4.46	86.37	2.84	88.93	1.47	95%
14SN-1-3-29	26.59	1181	1.80	0.01386	0.00021	0.08537	0.00284	0.04460	0.00153	0.00438	0.00013	0.45541	83.18	2.66	88.25	2.66	88.76	1.33	93%
14SN-1-3-30	16.07	688	1.91	0.01413	0.00024	0.09152	0.00354	0.04715	0.00189	0.00441	0.00014	0.43157	88.92	3.29	88.94	2.85	90.46	1.50	98%
Analysis	Pb	U	Th/U	Atomic Ratios								rho	Ages(Ma)						Concordance
	(ppm)			$^{206}Pb/^{238}U$	± 1σ	$^{207}Pb/^{235}U$	± 1σ	$^{207}Pb/^{206}Pb$	± 1σ	$^{208}Pb/^{232}Th$	± 1σ		$^{207}Pb/^{235}U$	± 1σ	$^{208}Pb/^{232}Th$	± 1σ	$^{206}Pb/^{238}U$	± 1σ	
14CM-3-1	2.75	142	1.17	0.01429	0.00039	0.08594	0.00645	0.04513	0.00381	0.00426	0.00021	0.36447	83.72	6.03	85.91	4.20	91.47	2.49	91%
14CM-3-2	5.16	283	0.69	0.01464	0.00026	0.09034	0.00609	0.04452	0.00306	0.00450	0.00018	0.26585	87.82	5.67	90.65	3.66	93.70	1.67	93%
14CM-3-3	6.21	263	0.54	0.01502	0.00033	0.08949	0.00537	0.04287	0.00244	0.00481	0.00022	0.36231	87.03	5.00	97.06	4.51	96.07	2.07	90%
14CM-3-4	3.45	180	0.49	0.01492	0.00034	0.09339	0.00491	0.04558	0.00256	0.00465	0.00023	0.43825	90.65	4.56	93.67	4.71	95.48	2.18	94%
14CM-3-5	7.54	73	0.39	0.02436	0.00059	0.16247	0.01509	0.04948	0.00523	0.00703	0.00055	0.25922	152.87	13.18	141.54	10.95	155.18	3.69	98%
14CM-3-6	5.69	298	0.83	0.01431	0.00029	0.10191	0.00527	0.05175	0.00277	0.00446	0.00019	0.38743	98.54	4.86	89.92	3.92	91.62	1.82	92%
14CM-3-7	3.87	210	0.63	0.01475	0.00037	0.08960	0.00601	0.04462	0.00323	0.00447	0.00024	0.37500	87.13	5.60	90.09	4.75	94.39	2.36	91%
14CM-3-8	5.76	315	0.76	0.01418	0.00026	0.09610	0.00482	0.04928	0.00257	0.00415	0.00018	0.37072	93.17	4.46	83.69	3.57	90.76	1.67	97%
14CM-3-9	3.71	206	0.55	0.01455	0.00036	0.09537	0.00662	0.04887	0.00390	0.00476	0.00028	0.35366	92.50	6.13	95.95	5.58	93.13	2.27	99%
14CM-3-10	4.74	252	0.66	0.01444	0.00031	0.09534	0.00570	0.04777	0.00269	0.00496	0.00023	0.35425	92.46	5.29	99.99	4.66	92.45	1.94	99%
14CM-3-11	6.44	334	0.77	0.01464	0.00042	0.10445	0.00585	0.05182	0.00268	0.00453	0.00024	0.51580	100.88	5.38	91.31	4.87	93.69	2.69	92%
14CM-3-12	5.53	284	0.69	0.01506	0.00051	0.15593	0.01910	0.06842	0.00603	0.00595	0.00053	0.27819	147.14	16.78	119.81	10.60	96.38	3.26	58%
14CM-3-13	4.79	276	0.62	0.01362	0.00025	0.08559	0.00494	0.04601	0.00279	0.00431	0.00023	0.32089	83.38	4.62	86.89	4.55	87.18	1.60	95%
14CM-3-14	7.75	377	1.02	0.01456	0.00029	0.10157	0.00522	0.05065	0.00255	0.00479	0.00017	0.39078	98.23	4.81	96.60	3.33	93.18	1.86	94%
14CM-3-15	3.98	219	0.72	0.01468	0.00047	0.10425	0.00951	0.05293	0.00487	0.00508	0.00026	0.34779	100.69	8.74	102.39	5.22	93.96	2.96	93%
14CM-3-16	2.61	143	0.50	0.01490	0.00038	0.08922	0.00730	0.04404	0.00361	0.00467	0.00034	0.31243	86.77	6.80	94.26	6.89	95.36	2.42	90%
14CM-3-17	6.24	327	0.73	0.01452	0.00021	0.10036	0.00505	0.05058	0.00279	0.00491	0.00020	0.28401	97.11	4.66	99.02	3.97	92.95	1.32	95%
14CM-3-18	2.87	157	0.63	0.01402	0.00026	0.09249	0.00534	0.04731	0.00247	0.00416	0.00016	0.31747	89.82	4.96	83.89	3.25	89.78	1.63	99%
14CM-3-19	4.99	272	0.70	0.01466	0.00029	0.09913	0.00546	0.04981	0.00295	0.00470	0.00020	0.35976	95.97	5.04	94.80	3.96	93.80	1.84	97%

(*continued on next page*)

Table 1 (*continued*)

Analysis	Pb	U	Th/U	Atomic Ratios								rho	Ages(Ma)						Concordance
	(ppm)			$^{206}Pb/^{238}U$	± 1σ	$^{207}Pb/^{235}U$	± 1σ	$^{207}Pb/^{206}Pb$	± 1σ	$^{208}Pb/^{232}Th$	± 1σ		$^{207}Pb/^{235}U$	± 1σ	$^{208}Pb/^{232}Th$	± 1σ	$^{206}Pb/^{238}U$	± 1σ	
14SN-1-3-1	18.50	846	1.63	0.01394	0.00025	0.08309	0.00328	0.04271	0.00184	0.00406	0.00014	0.45182	81.05	3.07	81.95	2.76	89.27	1.58	90%
14CM-3-20	3.19	342	0.77	0.01463	0.00027	0.09640	0.00552	0.04836	0.00274	0.00430	0.00017	0.32010	93.45	5.12	86.73	3.33	93.61	1.70	99%
14CM-3-21	6.01	337	0.60	0.01428	0.00030	0.08988	0.00560	0.04656	0.00304	0.00475	0.00019	0.33603	87.39	5.21	95.86	3.73	91.38	1.90	95%
14CM-3-22	3.83	216	0.58	0.01432	0.00031	0.08527	0.00580	0.04394	0.00323	0.00443	0.00026	0.31439	83.08	5.43	89.39	5.27	91.63	1.95	90%
14CM-3-23	4.22	117	0.83	0.01486	0.00033	0.08969	0.00522	0.04428	0.00278	0.00438	0.00020	0.37713	87.22	4.86	88.26	3.97	95.08	2.07	91%
14CM-3-24	6.87	168	0.51	0.01467	0.00034	0.09007	0.00566	0.04537	0.00299	0.00424	0.00020	0.37404	87.57	5.27	85.58	4.05	93.88	2.19	93%
14CM-3-25	3.24	176	0.58	0.01453	0.00037	0.09399	0.00742	0.04734	0.00375	0.00460	0.00023	0.31952	91.22	6.89	92.85	4.72	93.02	2.33	98%
14CM-3-26	6.35	351	0.62	0.01422	0.00029	0.09899	0.00476	0.05047	0.00242	0.00459	0.00020	0.42584	95.84	4.40	92.51	4.02	91.02	1.85	94%
14CM-3-27	2.34	251	0.88	0.01465	0.00033	0.09467	0.00624	0.04667	0.00296	0.00459	0.00021	0.34572	91.85	5.79	92.51	4.28	93.77	2.12	97%
14CM-3-28	7.14	372	0.99	0.01393	0.00030	0.09130	0.00495	0.04792	0.00268	0.00442	0.00016	0.39205	88.71	4.61	89.12	3.27	89.17	1.88	99%
14CM-3-29	7.49	380	0.86	0.01470	0.00028	0.10415	0.00535	0.05180	0.00278	0.00474	0.00016	0.36814	100.60	4.92	95.60	3.23	94.07	1.77	93%
14CM-3-30	7.16	376	0.87	0.01413	0.00023	0.09564	0.00481	0.04891	0.00240	0.00435	0.00017	0.31754	92.75	4.45	87.77	3.33	90.46	1.43	97%
Analysis	Pb	U	Th/U	Atomic Ratios								rho	Ages(Ma)						Concordance
	(ppm)			$^{206}Pb/^{238}U$	± 1σ	$^{207}Pb/^{235}U$	± 1σ	$^{207}Pb/^{206}Pb$	± 1σ	$^{208}Pb/^{232}Th$	± 1σ		$^{207}Pb/^{235}U$	± 1σ	$^{208}Pb/^{232}Th$	± 1σ	$^{206}Pb/^{238}U$	± 1σ	
SN-18-3-01	2.09	108	0.59	0.01469	0.00034	0.08308	0.00742	0.04208	0.00367	0.00434	0.00024	0.25548	81.04	6.95	87.58	4.80	94.04	2.13	85%
SN-18-3-02	1.35	68	0.50	0.01521	0.00036	0.09897	0.00751	0.04849	0.00367	0.00505	0.00032	0.31113	95.82	6.94	101.76	6.48	97.31	2.28	98%
SN-18-3-03	2.23	116	0.64	0.01438	0.00032	0.09133	0.00669	0.04652	0.00321	0.00463	0.00024	0.30025	88.74	6.23	93.39	4.78	92.03	2.01	96%
SN-18-3-04	3.23	162	0.64	0.01473	0.00028	0.09948	0.00605	0.04912	0.00297	0.00501	0.00021	0.31602	96.30	5.58	100.97	4.16	94.23	1.80	97%
SN-18-3-05	3.32	159	0.69	0.01514	0.00026	0.12367	0.00969	0.05877	0.00475	0.00502	0.00022	0.21848	118.40	8.76	101.20	4.39	96.90	1.65	80%
SN-18-3-06	2.32	121	0.64	0.01472	0.00031	0.09789	0.00775	0.04802	0.00359	0.00465	0.00023	0.26249	94.82	7.16	93.77	4.56	94.17	1.94	99%
SN-18-3-07	3.63	175	0.94	0.01458	0.00025	0.09450	0.00578	0.04741	0.00301	0.00459	0.00018	0.28233	91.69	5.37	92.65	3.53	93.32	1.60	98%
SN-18-3-08	2.27	106	0.69	0.01552	0.00035	0.12161	0.00993	0.05704	0.00469	0.00573	0.00027	0.27986	116.53	8.99	115.57	5.42	99.28	2.25	84%
SN-18-3-09	2.36	125	0.62	0.01425	0.00024	0.09449	0.00781	0.04848	0.00392	0.00464	0.00018	0.20604	91.68	7.24	93.57	3.68	91.24	1.54	99%
SN-18-3-10	2.45	114	0.66	0.01603	0.00038	0.11616	0.00727	0.05281	0.00315	0.00585	0.00028	0.37599	111.58	6.62	117.97	5.57	102.53	2.40	91%
SN-18-3-11	2.81	133	0.68	0.01577	0.00031	0.10337	0.00629	0.04750	0.00282	0.00523	0.00022	0.32158	99.88	5.79	105.53	4.44	100.88	1.96	99%
SN-18-3-12	3.13	152	0.70	0.01534	0.00031	0.10930	0.00720	0.05163	0.00331	0.00479	0.00024	0.31072	105.33	6.59	96.52	4.76	98.13	1.99	92%
SN-18-3-13	2.74	123	0.98	0.01567	0.00034	0.11164	0.00741	0.05276	0.00359	0.00515	0.00023	0.32651	107.46	6.76	103.75	4.65	100.23	2.15	93%
SN-18-3-14	1.76	92	0.69	0.01435	0.00030	0.10435	0.00782	0.05272	0.00386	0.00493	0.00026	0.27921	100.79	7.19	99.49	5.25	91.84	1.91	90%
SN-18-3-15	2.23	112	0.65	0.01490	0.00034	0.10687	0.00848	0.05182	0.00430	0.00475	0.00028	0.28469	103.10	7.78	95.79	5.63	95.36	2.14	92%
SN-18-3-16	3.11	148	0.71	0.01556	0.00030	0.10210	0.00754	0.04750	0.00338	0.00495	0.00021	0.26529	98.71	6.95	99.79	4.27	99.51	1.94	99%
SN-18-3-17	2.54	124	0.78	0.01491	0.00031	0.10457	0.00799	0.05182	0.00415	0.00490	0.00021	0.27603	100.99	7.35	98.77	4.31	95.40	2.00	94%
SN-18-3-18	2.09	108	0.67	0.01483	0.00035	0.10025	0.00752	0.04993	0.00369	0.00515	0.00026	0.31173	97.01	6.94	103.90	5.16	94.92	2.20	97%
SN-18-3-19	3.00	157	0.67	0.01475	0.00028	0.09779	0.00659	0.04888	0.00359	0.00447	0.00017	0.27725	94.74	6.09	90.13	3.51	94.36	1.75	99%
SN-18-3-20	1.91	105	0.69	0.01413	0.00029	0.09561	0.00699	0.04996	0.00378	0.00412	0.00018	0.28100	92.72	6.48	83.19	3.54	90.43	1.84	97%
SN-18-3-21	1.41	76	0.55	0.01486	0.00033	0.10334	0.00788	0.05257	0.00419	0.00472	0.00025	0.29521	99.85	7.25	95.10	5.08	95.08	2.12	95%
SN-18-3-22	2.80	138	0.68	0.01515	0.00030	0.10877	0.00778	0.05216	0.00368	0.00524	0.00020	0.28050	104.84	7.12	105.55	3.99	96.91	1.93	92%
SN-18-3-23	2.54	127	0.75	0.01503	0.00027	0.10119	0.00691	0.04939	0.00340	0.00472	0.00015	0.26395	97.87	6.38	95.21	3.09	96.15	1.72	98%
SN-18-3-24	2.04	112	0.67	0.01384	0.00028	0.09723	0.00668	0.05130	0.00343	0.00430	0.00019	0.29840	94.21	6.19	86.76	3.77	88.60	1.81	93%
SN-18-3-25	3.43	165	1.10	0.01436	0.00028	0.09875	0.00640	0.04979	0.00301	0.00432	0.00016	0.30202	95.62	5.91	87.21	3.16	91.89	1.79	96%
SN-18-3-26	2.71	136	0.72	0.01463	0.00030	0.10443	0.00686	0.05256	0.00348	0.00443	0.00019	0.31183	100.86	6.31	89.42	3.73	93.65	1.90	92%
SN-18-3-27	1.67	81	0.56	0.01538	0.00038	0.13374	0.01070	0.06268	0.00475	0.00513	0.00032	0.31259	127.45	9.59	103.50	6.35	98.37	2.44	74%
SN-18-3-28	3.08	148	0.73	0.01498	0.00029	0.10495	0.00710	0.05094	0.00335	0.00491	0.00019	0.28494	101.34	6.53	98.92	3.78	95.84	1.83	94%
SN-18-3-29	3.35	174	0.75	0.01446	0.00026	0.10517	0.00686	0.05348	0.00345	0.00430	0.00018	0.27779	101.54	6.31	86.73	3.60	92.56	1.67	90%
SN-18-3-30	2.79	143	0.65	0.01479	0.00028	0.09155	0.00560	0.04519	0.00278	0.00469	0.00022	0.30514	88.95	5.21	94.49	4.40	94.62	1.75	93%

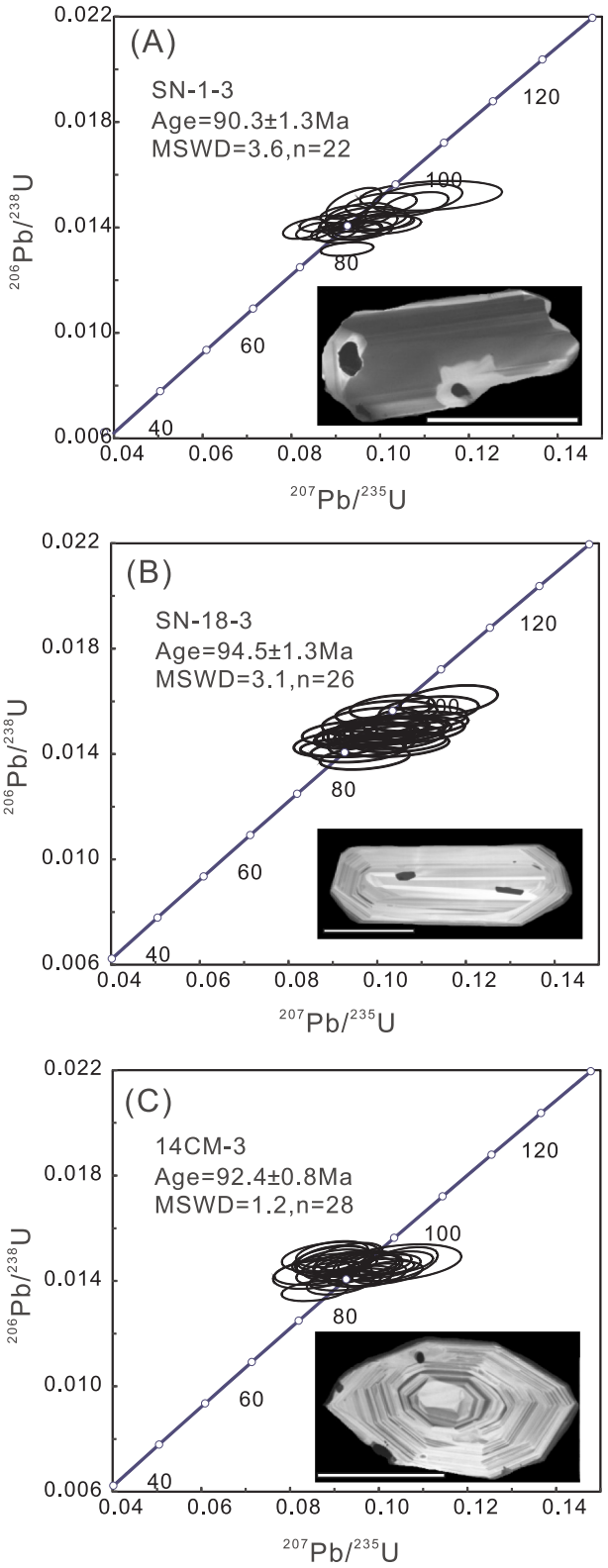

Fig. 4. Zircon LA–ICP–MS U–Pb concordia diagrams and associated CL images of representative zircons showing data for Kelu (A) and Sangbujiala (B–C) biotite granodiorite samples.

4.2. Molybdenite Re–Os isotopic compositions

A total of five samples from the Sangbujiala deposit and six samples from the Kelu deposit were dated using the molybdenite Re–Os method during this study. Molybdenite Re–Os isotopic analyses were performed using a Thermo X Series 2 ICP–MS instrument at SKLIG, GIGCAS, Guangzhou, China. Prior to analysis, molybdenite samples were digested using concentrated HNO_3 using a Carius tube approach and the analytical procedures outlined in Sun et al. (2010). Model Re–Os ages were calculated using ln ($^{187}Os/^{187}Re$ + 1)/λ and a decay constant (λ) of 1.666e^{-11} yr^{-1} (Smoliar et al., 1996). Isochron and weighted mean ages were calculated using the Isoplot/Ex_ver3 software package (Ludwig, 2003), and all uncertainties are reported as 2σ values.

4.3. Whole-rock geochemistry

The whole-rock geochemical compositions of two biotite granodiorite (14SN-1-2 and 14SN-1-3) and two diorite (14SN-3-2 and 14SN-3-6) samples from the Kelu deposit and a further three biotite granodiorite samples (14CM-2, 14CM-3, and 14CM-5) from the Sangbujiala deposit were determined during this study, with all analyses being undertaken at SKLIG, GIGCAS, Guangzhou, China. Prior to analysis, samples were crushed to pass a 200 mesh. Major-element contents were determined using a Rigaku RIX 2000 X-ray fluorescence spectrometer employing the techniques outlined in Li et al. (2005), yielding analytical uncertainties of 1%–5%. Trace-element contents were determined by ICP–MS employing a Perkin-Elmer Sciex ELAN 6000 instrument and the analytical approaches outlined in Li et al. (2002). Rhodium was used as an internal standard to monitor signal drift during counting, and the BHVO-2, GSR-1, GSR-2, GSR-3, AGV-2, W-2, and SARM-4 standards were used for calibration. The analytical precision for the majority of elements analyzed by ICP–MS is better than 3% in terms of relative standard deviation (RSD).

4.4. Whole-rock Sr–Nd isotopic analysis

The whole-rock Sr–Nd isotopic analysis undertaken during this study used the same samples as used for whole-rock geochemical analysis. This analysis was undertaken at the SKLIG, GIGCAS, Guangzhou, China. Sample solutions were prepared by dissolving whole-rock powders in a mixture of HF + HNO_3, with Sr and rare-earth elements (REEs) being separated from the resulting solutions using cation columns (Wei et al., 2002). Isotopic measurements were performed on a Neptune Plus MC–ICP–MS instrument equipped with nine Faraday cup collectors and eight ion counters (Li et al., 2002). Measured $^{87}Sr/^{86}Sr$ and $^{143}Nd/^{144}Nd$ ratios were normalized to $^{86}Sr/^{88}Sr$ = 0.1194 and $^{146}Nd/^{144}Nd$ = 0.7219, respectively. Repeat analysis of the NIST SRM 987 and Shin Etsu JNdi-1 standards yielded $^{87}Sr/^{86}Sr$ values of 0.71028 and $^{143}Nd/^{144}Nd$ values of 0.51209, respectively.

4.5. Zircon Hf isotopic analysis

The Lu–Hf isotopic compositions of zircons from one biotite granodiorite sample (14SN-1-3) from the Kelu deposit and one biotite granodiorite sample (SN-18-3) from the Sangbujiala deposit were determined during this study. This analysis was undertaken using a Thermo Finnigan Neptune MC–ICP–MS instrument coupled with a Resolution M50 LA system at the SKLIG, GIGCAS, Guangzhou, China. This analysis used 40-μm-diameter laser pits and an ablation time of 60 s with an energy of 15–20 J/cm^2 and a rate of 8 Hz. Details of the procedures used are given in Wu and Yang (2006). Measured $^{176}Hf/^{177}Hf$ values were normalized to $^{179}Hf/^{177}Hf$ = 0.7325, $^{176}Lu/^{175}Lu$ = 0.02655, and $^{176}Yb/^{172}Yb$ = 0.5887 (Chu et al., 2006; Wu et al., 2006). Repeat analysis of the Penglai standard zircon yielded a mean $^{176}Hf/^{177}Hf$ ratio of 0.282915 ± 0.000042 (2σ, n = 60), consistent with the recommended $^{176}Hf/^{177}Hf$ value for this standard (0.282906 ± 0.000010, 2σ; Li et al., 2010).

Table 2
Re-Os data for the molybdenite from Kelu and Sangbujiala Cu-Au deposits.

Sample No.	Concentration (ppb)								Model Age(Ma)	
	Re	± 1σ	Common Os	± 1σ	^{187}Re	± 1σ	^{187}Os	± 1σ	Age	± 1σ
KL-19-1	101,461	3858	0.49	0.03	63,514	2415	100.6	0.8	95.3	0.8
KL-19-2	136,326	2451	0.64	0.02	85,340	1534	138.0	0.5	97.3	0.4
KL-19-3	104,934	1553	2.49	0.06	65,689	972	107.0	0.9	98.1	0.8
KL-19-4	141,116	1568	1.79	0.09	88,339	982	144.8	2.6	98.7	1.8
KL-19-5	110,169	2461	2.37	0.07	68,966	1541	113.8	1.6	99.4	1.4
KL-19-6	138,739	795	1.23	0.09	86,850	497	136.9	1.6	94.9	1.1
SBJL-21-1	49,570	637	1.08	0.08	31,031	399	50.2	0.5	97.4	1.0
SBJL-21-2	21,891	397	0.43	0.03	13,704	249	22.0	0.1	96.6	0.5
SBJL-21-3	15,831	771	0.22	0.01	9910	482	16.4	0.4	99.4	2.3
SBJL-21-4	55,979	926	0.82	0.06	35,043	580	54.2	0.7	93.2	1.1
SBJL-21-5	29,581	273	0.88	0.04	18,518	171	28.5	0.2	92.6	0.6

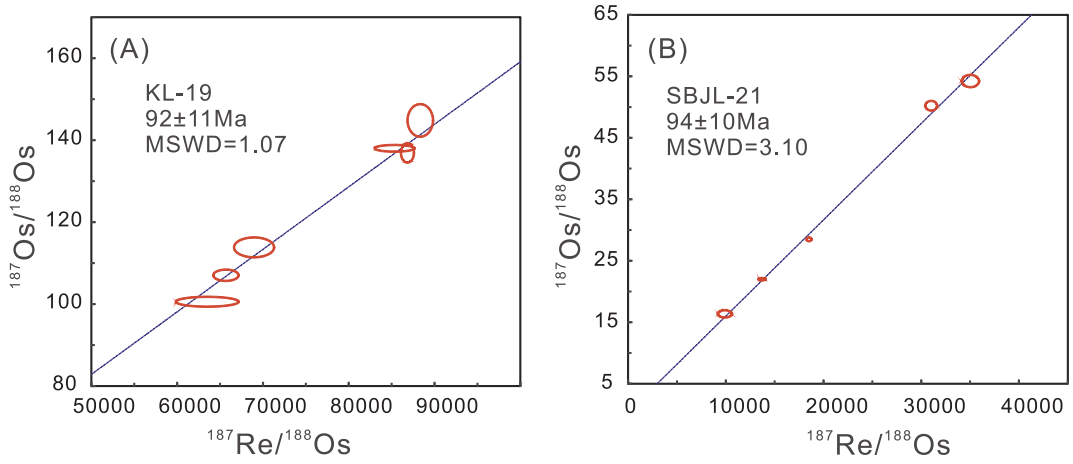

Fig. 5. Molybdenite Re–Os isochron diagrams for samples from the Kelu (A) and Sangbujiala (B) deposits.

5. Results

5.1. Zircon trace-element and U–Pb geochronological data

The zircons analyzed during this study appear homogeneous and show oscillatory zoning during CL imaging (Fig. 4). Their trace-element and U–Pb isotopic compositions are given in Supplemental Table 1 and Table 1, respectively.

The 30 analyzed zircons from Kelu biotite granodiorite sample SN-1-3 contain 188–1181 ppm U and have Th/U ratios of 0.64–2.23 (Table 1). Eight analyses with < 90% concordance were excluded from further consideration, with the remaining 22 zircons yielding U–Pb ages ranging from 88.60 ± 1.81 to 102.53 ± 2.40 Ma and a mean U–Pb age of 90.3 ± 1.3 Ma (MSWD = 3.6).

Thirty zircons from Sangbujiala biotite granodiorite sample SN-18 contain 68–165 ppm U and have Th/U ratios of 0.50–1.10 (Table 1). Twenty-six of these zircons have > 90% concordance and yield U–Pb ages ranging from 84.40 ± 1.09 to 97.27 ± 2.36 Ma and a weighted mean age of 94.5 ± 1.3 Ma (MSWD = 3.1).

A total of 30 zircons from Sangbujiala biotite granodiorite sample 14CM-3 included one zircon with < 90% concordance and one inherited zircon with an age of 96.07 ± 2.07 Ma, both of which were excluded from further consideration. The remaining 28 zircons contain 73–372 ppm U and have Th/U ratios of 0.51–1.17. They yield U–Pb ages from 87.18 ± 1.60 to 96.07 ± 2.07 Ma and a weighted mean age of 92.4 ± 0.8 Ma (MSWD = 1.2).

5.2. Molybdenite Re–Os isotopic data

The molybdenite Re–Os isotopic compositions of six samples from the Kelu deposit and five samples from the Sangbujiala deposit are given in Table 2 and are shown in Fig. 5. The six samples from the Kelu deposit contain 63,514–88,339 ppb ^{187}Re and 100.6–144.8 ppb ^{187}Os. They yield model ages that range from 94.9 ± 1.1 to 99.4 ± 1.4 Ma and a weighted mean age of 97.1 ± 1.3 Ma (MSWD = 3.0). These samples also yield an isochron age of 92 ± 11 Ma (MSWD = 1.07) that is within uncertainty of the weighted mean model age (Fig. 5A), suggesting that this molybdenite formed at ca. 92 Ma.

The five samples from the Sangbujiala deposit contain 9910–35,043 ppb ^{187}Re and 16.4–54.2 ppb ^{187}Os and yield model ages that range from 92.6 ± 0.6 to 99.4 ± 2.3 Ma with a weighted mean age of 95.2 ± 2.9 Ma (MSWD = 8.6). They also yield an isochron age of 94 ± 10 Ma (MSWD = 3.10) that is within uncertainty of the weighted mean model age (Fig. 5B), suggesting that the molybdenite in the Sangbujiala deposit formed at ca. 94 Ma.

5.3. Whole-rock major- and trace-element geochemistry

The whole-rock major- and trace-element compositions of the intrusions associated with the Kelu and the Sangbujiala deposits are given in Table 3. Two diorite samples from the Kelu deposit contain elevated contents of MgO (6.24 and 5.99 wt%) but low contents of SiO_2 (55.29 and 54.05 wt%), and K_2O (1.42 and 1.44 wt%), indicating that these samples are compositionally similar to the diorite and monzonite samples reported previously by Jiang et al. (2012). The biotite granodiorite samples contain elevated contents of SiO_2 (64.13 to 64.45 wt%) but low contents of MgO (2.51 to 2.83 wt%) relative to the other intrusive rocks within the Kelu district. However, both diorite and biotite granodiorite samples have high-K calc-alkaline affinities (Fig. 6) and are metaluminous with molar $Al_2O_3/(CaO + Na_2O + K_2O)$ (A/CNK)

Table 3
Major and trace elements compositions of the intrusions in Kelu and Sangbujiala deposits.

Sample No.	14CM-2	14CM-3	14CM-5	14SN-1-2	14SN-1-3	14SN-3-2	14SN-3-6-2
Rock type	Biotite granite (Sangbujiala)			Biotite granodiorite (Kelu)		Diorite (Kelu)	
Major element (wt. %)							
Al_2O_3	17.53	13.60	14.07	13.63	13.92	13.93	13.64
CaO	3.87	3.51	3.30	3.90	4.23	6.74	6.96
Fe_2O_3	3.90	4.85	4.27	6.69	7.37	14.00	15.32
K_2O	3.29	2.10	2.92	3.09	2.85	1.42	1.44
MgO	2.58	1.93	2.08	2.51	2.83	6.24	5.99
MnO	0.14	0.12	0.11	0.13	0.17	0.19	0.20
Na_2O	2.00	2.92	1.36	2.82	2.99	1.81	1.99
P_2O_5	0.15	0.15	0.15	0.16	0.16	0.13	0.14
SiO_2	64.78	69.47	70.03	64.45	64.13	53.01	51.93
TiO_2	0.76	0.53	0.58	0.86	0.92	1.21	1.20
L.O.I	0.63	0.57	0.67	1.42	0.24	1.07	0.92
Total	99.63	99.75	99.54	99.67	99.80	99.74	99.73
ACNK	1.16	0.93	1.13	0.84	0.82	0.74	0.70
$Mg^{\#}$	56.92	44.30	49.27	42.86	43.42	47.13	43.87
Trace elements (ppm)							
Li	15.4	11.3	21.5	15	14.2	21.4	21.3
Be	1.66	1.07	1.19	1.51	1.38	0.65	1.06
Sc	14.7	13.6	13.3	11.8	12.7	17.4	20.4
V	121	95.3	126	143	162	433	433
Cr	96.7	35.8	50.6	40.6	57.6	52.6	53.9
Co	8.54	11.8	10.5	17.8	20.6	47.2	42.1
Ni	15.6	32.2	32.4	27.8	29.6	95.2	78.2
Cu	11.2	94	13.1	80.3	103	489	126
Zn	64	72.4	53.1	103	90.6	140	126
Ga	17.4	16.6	18.9	18	17.8	19.2	20.2
Rb	149	95.5	158	102	84.6	66.5	62.5
Sr	416	1110	684	729	804	817	702
Y	18.6	9	7.96	16	15.6	11.3	21.6
Zr	117	65.3	94.7	148	92.7	44.9	53
Nb	9.61	4.78	5.49	7.85	7.96	4.2	7.27
Cs	17.4	9.63	13.4	6.96	3.39	5.79	9.78
Ba	443	440	390	442	441	136	125
La	30.1	22.5	26.2	28.4	28.9	12	23
Ce	61.9	40	45.8	56.5	57.1	26.3	52.9
Pr	7.36	4.8	5.22	7.01	6.9	3.45	6.9
Nd	28.3	17.2	20	26.1	25.2	13.6	25.7
Sm	5.23	2.92	3.47	4.97	5.05	3.04	5.51
Eu	1.21	0.89	0.90	1.24	1.26	0.87	1.19
Gd	4.11	2.29	2.36	3.53	3.75	2.46	4.61
Tb	0.61	0.34	0.33	0.5	0.54	0.35	0.67
Dy	3.07	1.58	1.46	2.84	2.93	2.05	3.96
Ho	0.54	0.32	0.28	0.57	0.55	0.39	0.78
Er	1.67	0.88	0.88	1.52	1.5	1.06	2.11
Tm	0.25	0.11	0.13	0.2	0.19	0.14	0.28
Yb	1.58	0.77	0.81	1.25	1.28	0.82	1.76
Lu	0.23	0.12	0.12	0.19	0.19	0.12	0.25
Hf	3.06	1.71	2.32	3.44	2.3	1.33	1.7
Ta	0.61	0.39	0.42	0.47	0.59	0.4	0.83
W	3.63	2.64	7.65	1.35	1.22	2.94	2.24
Tl	0.7	0.62	1.07	0.56	0.41	0.45	0.38
Pb	9.95	13.7	13	13.7	13.5	9.4	8.08
Bi	0.133	0.328	0.219	0.027	0.087	0.043	0.129
Th	12.77	6.01	9.23	10.33	7.37	4.46	4.73
U	3.45	1.91	2.05	2.67	2.19	0.99	3.22
La/Yb_N	13.67	20.96	23.20	16.30	16.20	10.50	9.37
Sr/Y	22.37	123.33	85.93	45.56	51.54	72.30	32.50

values of 0.70–0.84 and $Mg^{\#}$ (molar $Mg^{2+}/(Mg^{2+} + Fe^{2+}) \times 100$) ratios of 43.4–47.1. They also have similar trace-element compositions characterized by small Eu anomalies ($Eu_N/Eu^* = 0.72–0.98$), light REE (LREE) enrichments ($[La/Yb]_N = 9.4–16.3$; Fig. 7B), and positive Sr and negative Nb, Ta, and Ti anomalies (Fig. 7A). They contain high contents of Sr (702–817 ppm) and low contents of Y (11.3–21.6 ppm) and Yb (0.82–1.76 ppm) that yield high Sr/Y ratios (32.5–72.3) similar to those found in adakitic rocks (Fig. 8A; Defant and Drummond, 1993).

The three Sangbujiala biotite granodiorite samples contain consistent contents of SiO_2 (64.78–70.03 wt%) and are classified as calc-alkaline (Fig. 6). They contain 1.93–2.58 wt% MgO, have $Mg^{\#}$ values of 44.3–56.9, contain relatively high contents of Al_2O_3 (17.53–13.06 wt %), and have A/CNK values of 0.93–1.16. Their primitive-mantle-normalized multi-element variation diagram patterns show enrichment in large-ion lithophile elements (LILEs) but depletion in high-field-strength elements (HFSEs) (Fig. 7A). They have slightly negative to positive Eu anomalies ($Eu_N/Eu^* = 0.80–1.05$), are enriched in LREEs ($[La/Yb]_N = 13.7–23.2$; Fig. 7B), are depleted in Nb and Ta, and contain low contents of Y that yield high Sr/Y ratios (22.4–123) indicative of an adakitic affinity (Fig. 8A).

5.4. Whole-rock Sr–Nd isotopic data

The whole-rock Sr and Nd isotopic compositions of the samples from

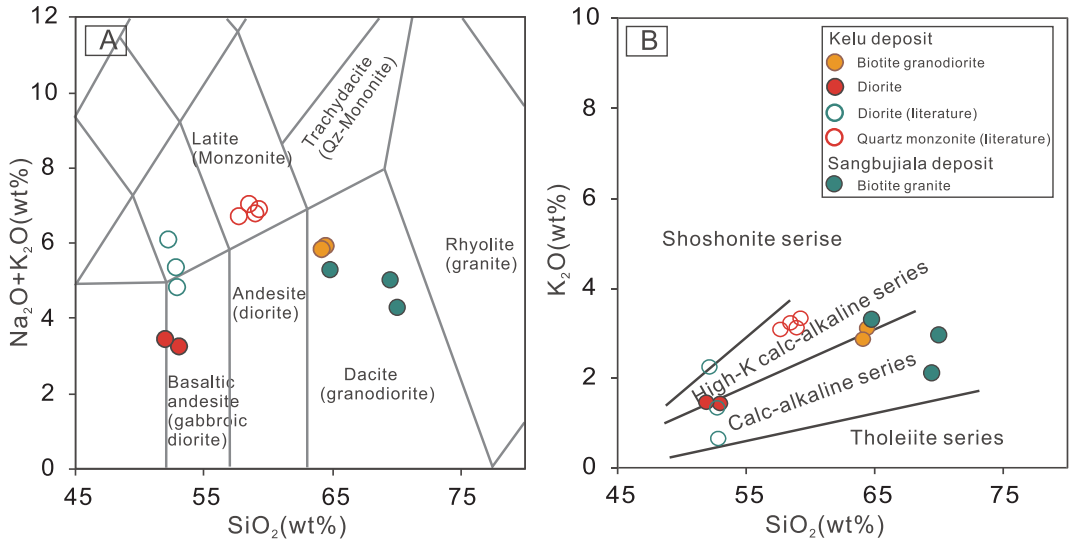

Fig. 6. (A) Na_2O + K_2O vs.SiO_2 (wt.%) (Middlemost, 1994) and (B) K_2O vs. SiO_2 (wt.%) (Peccerillo and Taylor, 1976) diagrams. Data for the Kelu diorites and quartz monzonites are from Jiang et al. (2012).

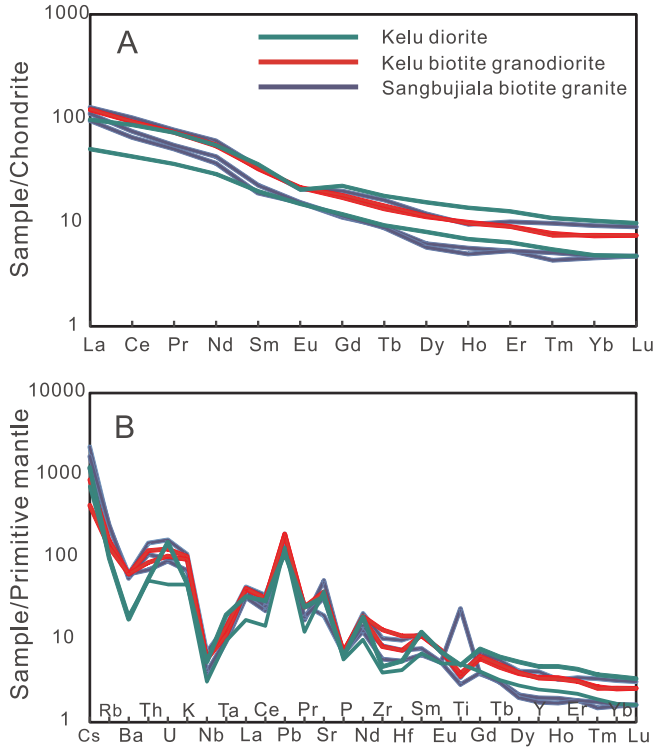

Fig. 7. (A) Chondrite-normalized REE and (B) primitive-mantle-normalized multi-element variation diagrams for intrusions associated with the Kelu and Sangbujiala Cu–Au deposits. Normalizing values are from Sun and McDonough (1989), and data sources are as in Fig. 6.

the Kelu–Sangbujiala area analyzed during this study are given in Table 4 and are shown in Fig. 9. The diorite and biotite granodiorite samples associated with the Kelu deposit have similar Sr–Nd isotopic compositions with consistent $(^{87}Sr/^{86}Sr)_i$ ratios (0.7042–0.7044) and $\varepsilon_{Nd}(t)$ values of 4.41–4.81, yielding two-stage model ages (T_{DM2}) of 530–498 Ma. The biotite granodiorites associated with the Sangbujiala deposit have $(^{87}Sr/^{86}Sr)_i$ ratios of 0.7040–0.7041, $\varepsilon_{Nd}(t)$ ratios of 3.99–4.02, and T_{DM2} ages of 566–556 Ma.

5.5. Zircon Hf isotopic data

The Hf isotopic data for zircons from the Kelu biotite granodiorite (14SN-1–3) and the Sangbujiala biotite granodiorite (14CM-3) are given in Table 5 and are shown in Fig. 9. A total of 15 zircons from the Kelu biotite granodiorite (14SN-1–3) yielded $^{176}Hf/^{177}Hf$ ratios of 0.2830–0.2831 and $\varepsilon_{Hf}(t)$ values of 8.02–13.18 calculated using a weighted mean U–Pb age of 90.3 Ma. These zircons have associated Hf T_{DM2} ages of 641–310 Ma. A further 15 zircons from the Sangbujiala biotite granodiorite (14CM-3) yielded $^{176}Hf/^{177}Hf$ ratios of 0.282945–0.283018 and $\varepsilon_{Hf}(t)$ values of 8.10–11.50 calculated using a weighted mean U–Pb age of 92.4 Ma. These zircons have associated Hf T_{DM2} ages of 637–419 Ma.

6. Discussion

6.1. Timing of formation of the Kelu Cu–Au and Sangbujiala Cu–Au deposits

The biotite granodiorite associated with the Kelu Cu–Au deposit yielded a zircon U–Pb age of 90.3 ± 1.3 Ma that is within uncertainty of the age of a diorite in this area (90.3 ± 2.1 Ma) and is similar to the age of a quartz monzonite (93.3 ± 2.0 to 91.3 ± 1.6 Ma) that also crops out in this area (Jiang et al., 2012). This suggests that the magmatism in the Kelu area occurred during the Late Cretaceous. Samples from the deposit also yield a molybdenite Re–Os isochron age of ca. 92 Ma, which is consistent with the zircon U–Pb ages of the intrusions in this area. Combining these data with the close spatial association of the intrusion and skarn mineralization in this area suggests that the Kelu Cu–Au mineralization formed as a result of the Late Cretaceous magmatism in this area.

Our zircon U–Pb dating of the biotite granodiorite associated with the Sangbujiala Cu–Au deposit yielded ages of 94.5 ± 1.3 and 92.4 ± 0.8 Ma that are within uncertainty of each other, suggesting that this intrusion was emplaced during the Late Cretaceous. The molybdenite samples from this deposit yielded a weighted mean Re–Os age of 95.2 ± 2.9 Ma that is similar to the zircon U–Pb ages for the biotite granodiorite in this area. This suggests that the Cu–Au mineralization in this area formed at the same time as the emplacement of the biotite granodiorite, with both occurring at ca. 95 Ma.

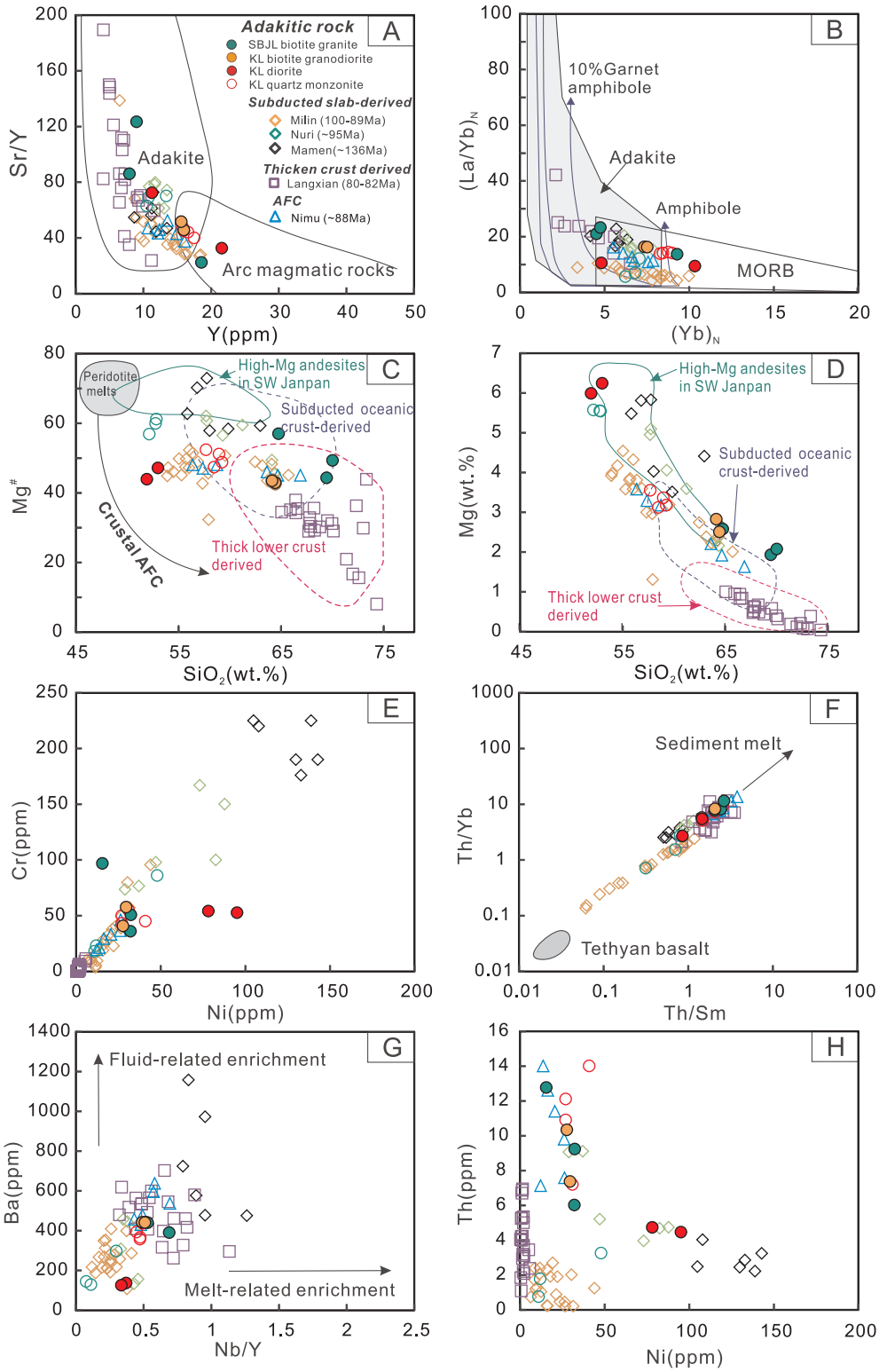

Fig. 8. Diagrams showing variations in (A) Sr/Y vs. Y (Defant and Drummond, 1993), (B) $(La/Yb)_N$ vs. Yb_N, (C) $Mg^{\#}$ vs. SiO_2, (D) MgO vs. SiO_2, (E) Cr vs. Ni, (F) Th/Yb vs. Th/Sm, (G) Ba vs. Nb/Y, and (H) Th vs. Ni within samples from the study area. Also shown are adakitic rocks from the Langxian (Wen et al., 2008; Zheng et al., 2014), Milin (Ma et al., 2013a, 2013b), Nimu (Xu et al., 2015), Mamen (Zhu et al., 2009), and Nuri (Zheng et al., 2014) areas.

6.2. Genesis of fertile adakitic rocks associated with the Kelu and Sangbujiala Cu–Au deposits

6.2.1. Petrogenesis of adakitic rocks in the Kelu and Sangbujiala areas

The Cretaceous diorite, quartz monzonite, and biotite granodiorite intrusions associated with the Kelu Cu–Au deposit and the biotite granodiorite associated with the Sangbujiala Cu–Au deposit all contain high contents of Sr and have high Sr/Y and La/Yb ratios, suggesting that these units have adakitic affinities (Fig. 8A and B). Previous research has indicated that the magmas that form adakitic rocks can be generated by (1) partial melting of subducted oceanic slab material (Defant and Drummond, 1993), (2) fractional crystallization of basaltic

Table 4
Bulk Sr-Nd isotopic compositions of the intrusions in Kelu and Sangbujiala Cu-Au deposits.

Sample	$^{87}Rb/^{86}Sr$	$^{87}Sr/^{86}Sr$	2 σ	$(^{87}Sr/^{86}Sr)_i$	$^{147}Sm/^{144}Nd$	$^{143}Nd/^{144}Nd$	2 σ	$(^{143}Nd/^{144}Nd)_{CHUR}$	$(^{143}Nd/^{144}Nd)_i$	ε_{Nd} (t)	$T_{DM,2}$(Ma)
Kelu											
14SN-1-2	0.404701	0.704406	0.000040	0.703888	0.115127	0.512836	0.000028	0.512522	0.512769	4.81	498
14SN-1-3	0.304348	0.704282	0.000071	0.703893	0.121157	0.512833	0.000027	0.512522	0.512761	4.66	509
14SN-3-2	0.235424	0.704161	0.000059	0.703860	0.135143	0.512828	0.000042	0.512522	0.512748	4.41	530
14SN-3-6	0.257510	0.704159	0.000066	0.703829	0.129621	0.512826	0.000026	0.512522	0.512750	4.44	527
Sangbujiala											
14CM-2	1.036064	0.705156	0.000073	0.703802	0.111730	0.512793	0.000019	0.512520	0.512726	4.02	564
14CM-3	0.248852	0.704375	0.000057	0.704050	0.102638	0.512786	0.000030	0.512520	0.512724	3.99	566
14CM-5	0.668162	0.704865	0.000052	0.703992	0.104895	0.512794	0.000030	0.512520	0.512731	4.12	556

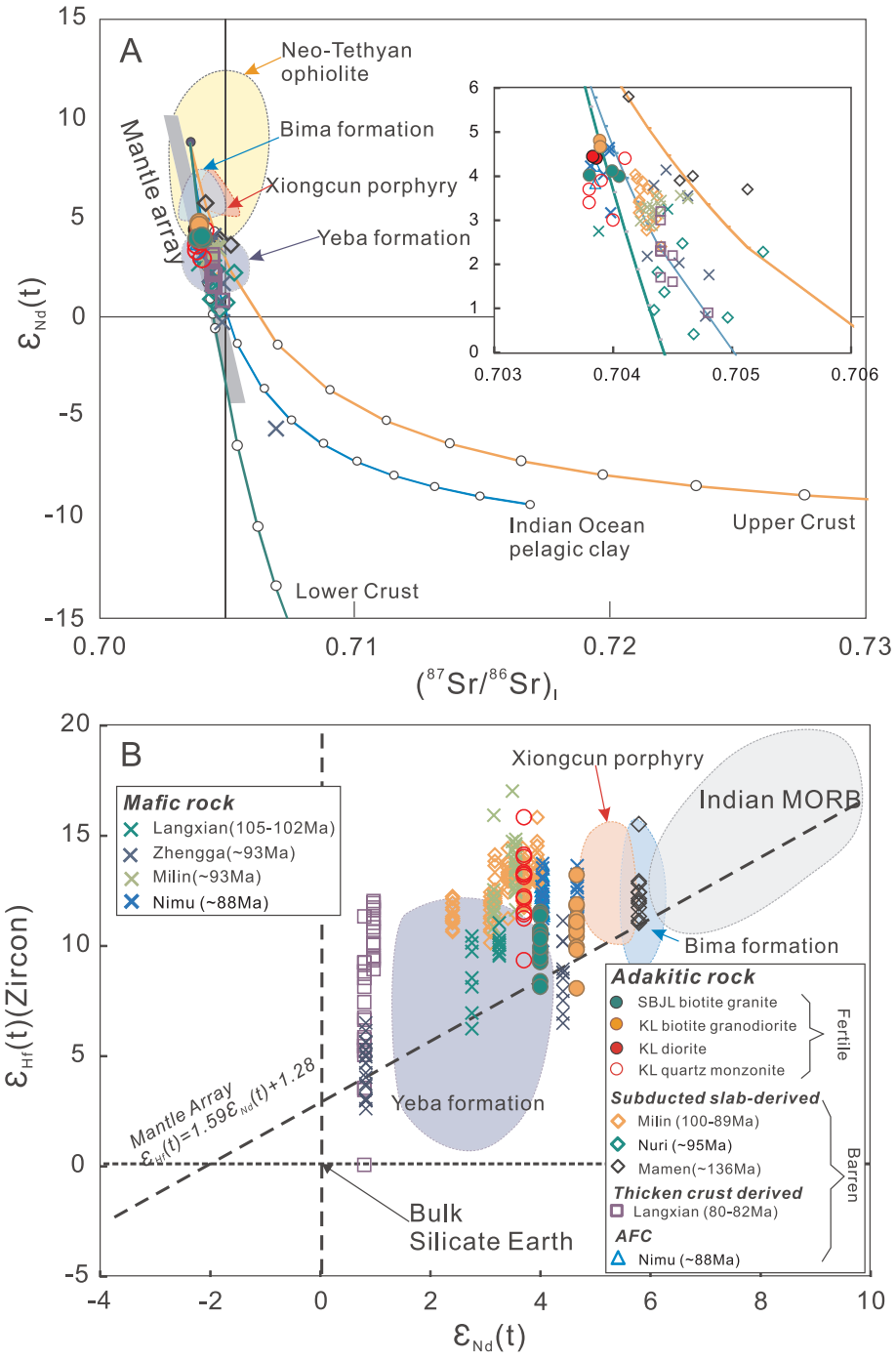

Fig. 9. (A) $\varepsilon_{Nd}(t)$ vs. $(^{87}Sr/^{86}Sr)_i$ and (B) zircon $\varepsilon_{Hf}(t)$ vs. $\varepsilon_{Nd}(t)$ diagrams for intrusions associated with the Kelu and Sangbujiala Cu–Au deposits. Data sources for (A) include ophiolite data from Mahoney et al. (1998), Xu and Castillo (2004), and Zhang et al. (2005), and Indian Ocean pelagic sediment data from Ben Othman et al. (1989). Data sources for (B) include Indian MORB from Ingle et al. (2003) and the mantle array from Chauvel and Blichert-Toft (2001). The Nd and Hf isotopic data for the Langxian adakitic rocks are from Wen et al. (2008) and Zheng et al. (2014). Also shown are data for adakitic and mafic rocks from the Milin (Ma et al., 2013a, 2013b) and Nimu (Xu et al., 2015) areas, adakitic rocks from the Mamen (Zhu et al., 2009) and Nuri (Zheng et al., 2014) areas, and mafic rocks from the Zhengga area (Ma et al., 2013c), as well as data fields for the Xiongcun deposit (Tang et al., 2015), the Bima Formation (Chen et al., 2019a), and the Yeba Formation (Liu et al., 2018).

Table 5
Zircon Lu-Hf isotopic composition of the intrusions from Kelu and Sangbujiala Cu-Au deposits.

Sample	Age(Ma)	$^{176}Lu/^{177}Hf$	$^{176}Hf/^{177}Hf$	2 σ Err.	$(^{176}Hf/^{177}Hf)i$	$(^{176}Hf/^{177}Hf)_{CHUR}$	$\varepsilon_{Hf}(0)$	$\varepsilon_{Hf}(t)$	$f_{(Lu/Hf)}$	T_{DM}(Ma)	$T_{DM,2}$(Ma)
Kelu diorite											
14SN-1-3-2	90	0.001783	0.283012	0.000010	0.283009	0.282716	8.50	10.37	−0.95	347	490
14SN-1-3-3	90	0.000884	0.283021	0.000009	0.283019	0.282716	8.79	10.72	−0.97	327	468
14SN-1-3-4	90	0.001513	0.283052	0.000010	0.283049	0.282716	9.89	11.78	−0.95	288	400
14SN-1-3-5	90	0.001568	0.283027	0.000009	0.283024	0.282716	9.01	10.89	−0.95	324	457
14SN-1-3-6	90	0.000552	0.282997	0.000012	0.282996	0.282716	7.97	9.91	−0.98	357	520
14SN-1-3-7	90	0.001798	0.283054	0.000011	0.283051	0.282716	9.97	11.84	−0.95	286	396
14SN-1-3-8	90	0.000682	0.282997	0.000011	0.282996	0.282716	7.96	9.90	−0.98	358	521
14SN-1-3-9	90	0.001510	0.283029	0.000009	0.283026	0.282716	9.08	10.97	−0.95	320	452
14SN-1-3-10	90	0.002491	0.283037	0.000010	0.283033	0.282716	9.38	11.21	−0.92	317	436
14SN-1-3-12	90	0.001033	0.283091	0.000008	0.283089	0.282716	11.26	13.18	−0.97	228	310
14SN-1-3-13	90	0.000399	0.282944	0.000013	0.282943	0.282716	6.07	8.02	−0.99	430	641
14SN-1-3-14	90	0.001406	0.283019	0.000009	0.283016	0.282716	8.72	10.62	−0.96	334	474
14SN-1-3-15	90	0.001785	0.282996	0.000010	0.282993	0.282716	7.91	9.78	−0.95	371	528
14SN-1-3-17	90	0.001079	0.283030	0.000010	0.283029	0.282716	9.14	11.05	−0.97	315	447
Sangbujiala biotite granite											
SN-18-3-1	92.1	0.000606	0.282952	0.000012	0.282951	0.282715	6.36	8.34	−0.98	421	622
SN-18-3-2	92.1	0.000547	0.283041	0.000010	0.283040	0.282715	9.51	11.50	−0.98	295	419
SN-18-3-3	92.1	0.000776	0.283011	0.000010	0.283009	0.282715	8.44	10.42	−0.98	340	489
SN-18-3-4	92.1	0.000646	0.283015	0.000010	0.283014	0.282715	8.60	10.58	−0.98	333	478
SN-18-3-5	92.1	0.000719	0.283018	0.000010	0.283017	0.282715	8.69	10.67	−0.98	329	473
SN-18-3-6	92.1	0.000467	0.283038	0.000007	0.283037	0.282715	9.40	11.39	−0.99	299	426
SN-18-3-7	92.1	0.000442	0.283036	0.000009	0.283035	0.282715	9.33	11.33	−0.99	302	431
SN-18-3-8	92.1	0.000682	0.282977	0.000009	0.282975	0.282715	7.24	9.22	−0.98	387	566
SN-18-3-9	92.1	0.000443	0.282989	0.000011	0.282988	0.282715	7.68	9.67	−0.99	367	536
SN-18-3-10	92.1	0.000614	0.283018	0.000010	0.283017	0.282715	8.69	10.68	−0.98	329	472
SN-18-3-11	92.1	0.000797	0.282982	0.000012	0.282981	0.282715	7.43	9.41	−0.98	380	553
SN-18-3-12	92.1	0.000811	0.283011	0.000010	0.283010	0.282715	8.46	10.44	−0.98	339	488
SN-18-3-13	92.1	0.000619	0.282945	0.000011	0.282944	0.282715	6.11	8.10	−0.98	431	637
SN-18-3-14	92.1	0.000694	0.282996	0.000010	0.282995	0.282715	7.92	9.90	−0.98	360	522
SN-18-3-15	92.1	0.000766	0.283006	0.000010	0.283005	0.282715	8.29	10.27	−0.98	346	498

magma (e.g., Castillo, 2012; Castillo et al., 1999; Wang et al., 2019; Xu et al., 2015), (3) partial melting of a thickened or delaminated region of the lower continental crust (Atherton and Petford, 1993; Kay and Kay, 1993; R. Wang et al., 2014; X. S. Wang et al., 2014), or (4) mixing of mafic and felsic magmas (Streck et al., 2007).

Mixing models require mantle-derived basaltic and crust-derived felsic magma end-members. The mantle-derived basaltic end-member is present in this region in the form of 95–90 Ma mafic rocks (e.g., the Milin and Zhengga mafic rocks; Fig. 9). However, the adakitic rocks in the Kelu and Sangbujiala areas have higher $\varepsilon_{Nd}(t)$ (3.99–4.81) and lower $(^{87}Sr/^{86}Sr)_i$ (0.7038–0.7041) values than those of the contemporaneous (ca. 94–91 Ma) basaltic rocks in the Zhengga and Milin areas ($\varepsilon_{Nd}(t)$ = −2.9 to 4.1, $(^{87}Sr/^{86}Sr)_i$ = 0.7042–0.7048; Ma et al., 2013a, 2013b; Table 4; Fig. 9), meaning that they cannot have formed as a result of magma mixing. Instead, it is likely that the adakitic rocks in this area formed from mantle-derived basaltic melts that were derived from a source region relatively free of crustal contamination. In addition, these adakitic rocks have $\varepsilon_{Nd}(t)$ values that do not correlate with changes in SiO_2 content (Fig. 10A), again indicating that they cannot have formed as a result of magma mixing.

It is also unlikely that the adakitic rocks in the Kelu and Sangbujiala areas formed from magmas generated by partial melting of a delaminated or thickened region of the lower crust. Adakitic rocks formed by this process usually have relatively low $\varepsilon_{Nd}(t)$ and high $(^{87}Sr/^{86}Sr)_i$ values, contrasting with the compositions of the rocks in the study area (Fig. 9A). The ca. 82–80 Ma Lilong and Langxian adakitic rocks of the southern Gangdese belt are thought to have formed as a result of partial melting of a thickened region of the lower crust within the garnet stability field, leaving residual garnet (Wen et al., 2008a; Zheng et al., 2014). Adakitic rocks formed by this process usually contain relatively low contents of MgO (< 1.0 wt%) and have low $Mg^{\#}$ values (31–37), similar to experimental melts derived from metabasalts under high-pressure and high-temperature (high-P–high-T) conditions (Fig. 8C and 8D, Rapp and Watson, 1995; Rapp et al., 1999). These adakitic rocks also typically contain low contents of Ni (0.4–5.8 ppm) and Cr (< 11.4 ppm; Guan et al., 2012; Macpherson et al., 2006) and have high Sr/Y ratios (Wen et al., 2008a; Zheng et al., 2014), contrasting with the higher $Mg^{\#}$ values (43–61) and Ni (11.0–95.2 ppm) and Cr (18.0–96.7 ppm) contents of the Kelu and Sangbujiala adakitic rocks.

High-pressure crystallization of basaltic magmas in the garnet stability field would generate melts with low concentrations of Y and HREEs but with elevated Sr/Y and $(Dy/Yb)_N$ ratios that are positively correlated with SiO_2 concentrations (e.g., Li et al., 2009; Wang et al., 2014a,b). However, these characteristics are not present within the adakitic Kelu and Sangbujiala samples (Fig. 7A and 10G). These types of adakitic rocks are thought to form as a result of fractional crystallization of amphibole combined with removal of plagioclase from a water-rich magma (e.g., Richards, 2011; Wang et al., 2014a,b). The adakitic rocks in the Kelu and Sangbujiala areas have MgO, Fe_2O_3, and CaO contents that are negatively correlated with SiO_2 contents, suggesting that they formed from magmas that fractionated mafic minerals prior to their emplacement (Fig. 10C and D). These samples also define positive and flat trends on $(Dy/Yb)_N$ and $(La/Sm)_N$ vs. SiO_2 diagrams, respectively (Fig. 10G and H), both of which are consistent with amphibole fractionation (Tiepolo et al., 2007). The high Sr contents within these samples (Fig. 10E), combined with an absence of negative Eu anomalies (Fig. 10F), also reflect removal of plagioclase during the early stages of the evolution of these magmas. This suggests that fractional crystallization under hydrous conditions can explain at least part of the adakitic affinities of the Cretaceous intrusions in the Kelu and Sangbujiala areas. However, it is more likely that the dominant process that generated the magmas that formed these intrusions was melting of subducted oceanic slab material. This is consistent with the fact that these rocks have more primitive Sr and Nd isotopic compositions compared with contemporaneous mafic or felsic rocks in this area. These compositions are similar to those of samples from Neo-Tethyan ophiolites (Fig. 9), suggesting that the intrusions in the study area are slab-derived adakitic rocks. The adakitic rocks in the Sangbujiala and

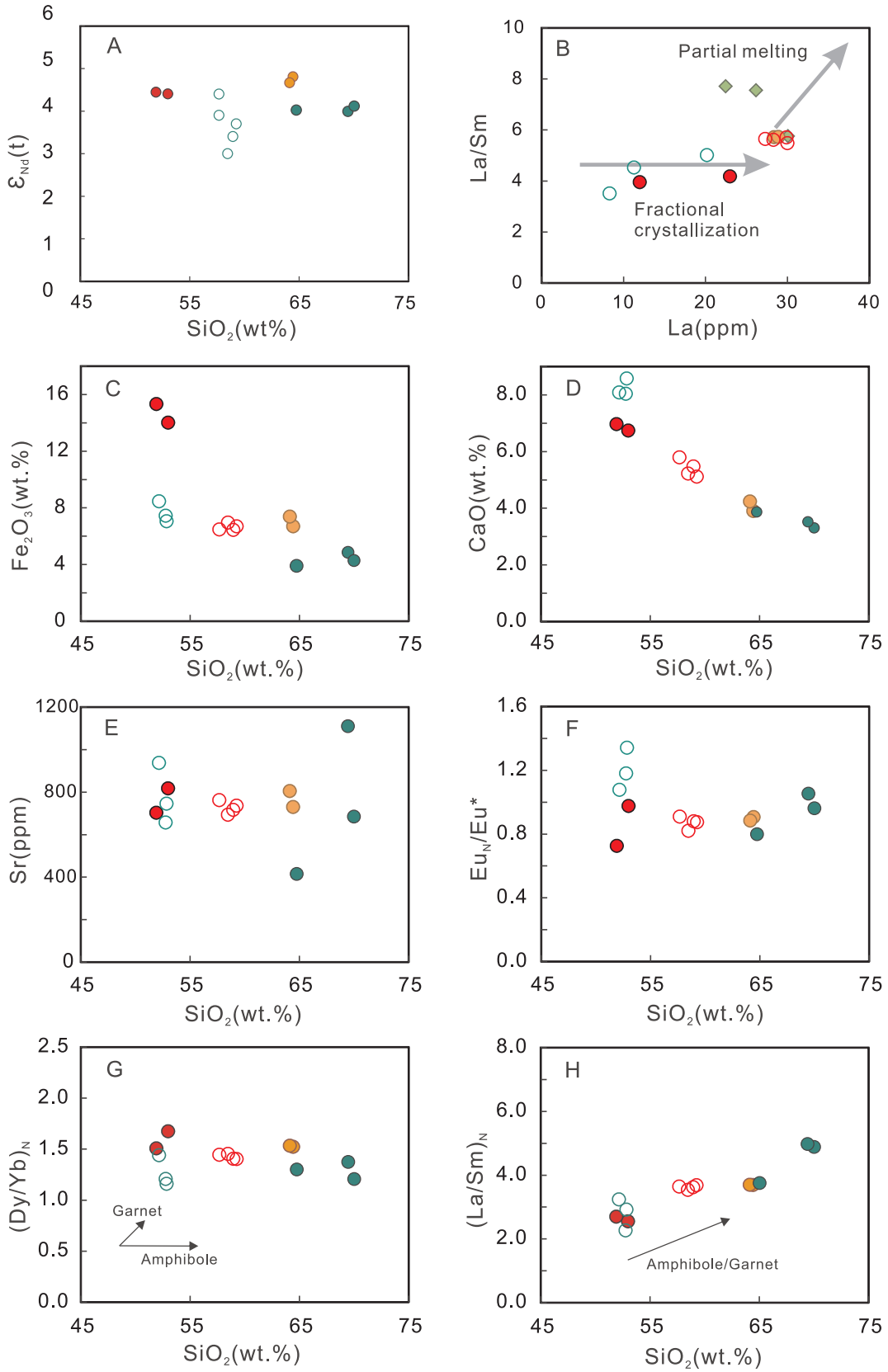

Fig. 10. Diagrams showing variations in (A) Fe_2O_3 vs. SiO_2, (B) La/Sm vs. La, (C) Fe_2O_3 vs. SiO_2, (D) CaO vs. SiO_2, (E) Sr vs. SiO_2. (F) Eu_N/Eu^* vs. SiO_2. (G) $(Dy/Yb)_N$ vs. SiO_2, and (H) $(La/Sm)_N$ vs. SiO_2, with symbols as shown in Fig. 6.

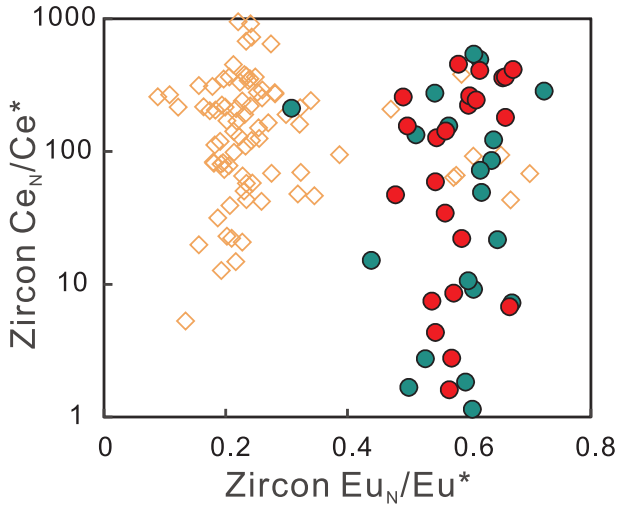

Fig. 11. Diagram showing variations in zircon Ce^{4+}/Ce^{3+} vs. Eu_N/Eu^* values, with data for barren adakitic rocks from Zhang et al. (2010). Symbols are as in Fig. 9.

Kelu areas also have relatively high $Mg^{\#}$ values (42.9–61.2, Fig. 8C and D) compared with slab-derived adakitic melts (generally < 50, Martin and Moyen, 2002; Shimoda et al., 1998), suggesting that the magmas that formed these intrusions interacted with mantle wedge peridotites during their ascent (Rapp et al., 1999).

In summary, the adakitic rocks in the Kelu and Sangbujiala areas formed from magmas generated by partial melting of Neo-Tethyan subducted slab material that subsequently interacted with overlying mantle wedge peridotite material. These magmas were water rich and fractionated amphibole and plagioclase during the early stages of their evolution, with the latter mineral being removed from the system.

6.2.2. Geochemical characteristics controlling the fertility of Cretaceous adakitic rocks

Numerous Cretaceous intrusions within the Gangdese batholith have adakitic affinity, including adakitic rocks in the Mamen (ca. 136 Ma; Zhu et al., 2009), Sangri (ca. 95 Ma; Zhang et al., 2019), Nuri (ca. 95 Ma; Zheng et al., 2014), Lilong (ca. 88 Ma; Zhang et al., 2010), Nimu (ca. 88 Ma; Xu et al., 2015), and Milin (ca. 100–89 Ma; Ma et al., 2013a, 2013c) areas. However, these intrusions are associated with very minor amounts of mineralization (Jiang et al., 2012), meaning that the differences between fertile and barren adakitic rocks (from a metallogenic sense) remain unclear.

The Sangbujiala and Kelu fertile rocks have higher $\varepsilon_{Nd}(t)$ but lower zircon $\varepsilon_{Hf}(t)$ ratios than those of the barren adakitic rocks mentioned above, indicating that the former rocks record significant Nd–Hf decoupling (Fig. 9B). Previous research indicates that low Lu/Hf zircons are generally indicative of residual weathered sources that generated clays containing anomalously radiogenic Hf (Vervoort et al., 1999). The

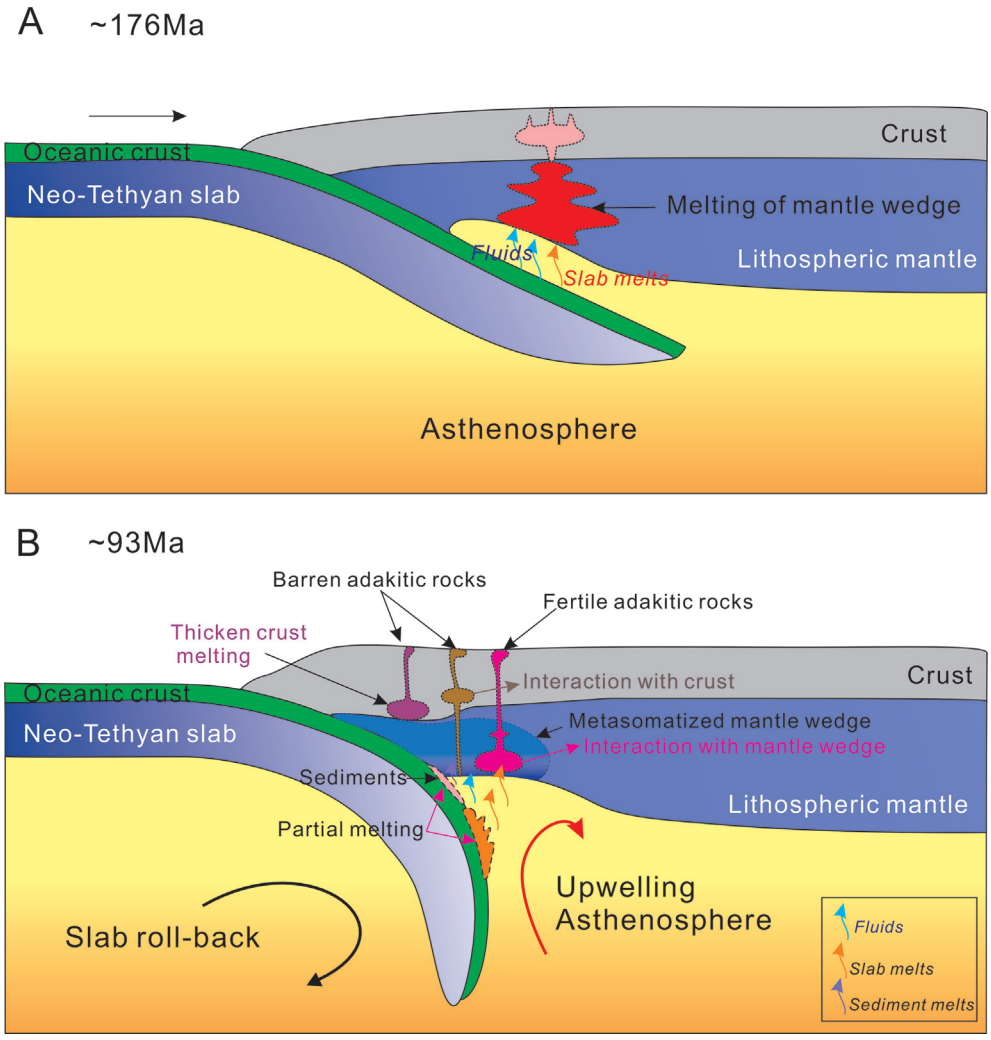

Fig. 12. Model depicting the generation of Jurassic and Cretaceous adakitic magmas within the southern Gangdese belt.

addition of sediment-derived melts to source regions should generate magmas with lower whole-rock $\varepsilon_{Nd}(t)$ ratios and higher $\varepsilon_{Hf}(t)$ values (Vervoort and Patchett, 1996). In addition, both Ma et al. (2013a) and Zheng et al. (2014) have suggested that the barren adakitic rocks of the Milin and Nuri areas formed from magmas that interacted with sediment-derived melts or fluids (Ma et al., 2013a, 2013c; Zheng et al., 2014).

The adakitic rocks in the Sangbujiala and Kelu areas have less Nd–Hf decoupling compared with those of the barren adakitic rocks (Fig. 9B), suggesting that they are derived from sources containing smaller amounts of sedimentary material compared with the sources of the barren adakitic rocks in these areas. However, these fertile adakitic rocks contain relatively high contents of Th (mean Th/Yb = 6.02), consistent with derivation from melts containing sediment-derived components (> 2; Ben Othman et al., 1989; Nebel et al., 2007; Woodhead et al., 2001). This is likely to reflect interaction of the parental magmas for these intrusions with overlying metasomatized mantle wedge material during their ascent.

Mantle wedge material becomes metasomatized and geochemically enriched as a result of interaction with slab-derived fluids and partial melts derived from sediments (Elburg et al., 2002; Guo et al., 2005). Interaction with the former usually increases the concentrations of fluid-mobile elements (e.g., Ba, Rb, Sr, U, and Pb) within source regions, whereas the latter commonly generates Th and LREE enrichments (e.g., Plank, 2005). The fertile adakitic rocks within the Sangbujiala and Kelu areas have elevated $Mg^{\#}$ ratios (Fig. 8C) and Ni and Cr contents (Fig. 8E) and have the most radiogenic Nd isotopic compositions (Fig. 9A) of all of the contemporaneous intrusions within this region. This suggests that these intrusions formed from parental magmas that interacted significantly with mantle wedge peridotite material prior to emplacement, with the former inheriting high Th concentrations from the latter, which was previously metasomatized by interaction with sediment-derived melts generated during earlier subduction.

The zircons within the Sangbujiala and Kelu adakitic rocks have mean Eu_N/Eu^* ratios of 0.53 and 0.58 (Fig. 11A), respectively, both of which are much higher than the values obtained from barren adakitic rocks in the Linong area (average $Eu_N/Eu^* = 0.25$; Zhang et al., 2010). This suggests that the fertile adakitic rocks are derived from magmas formed under higher magmatic oxygen fugacity conditions than those of the barren adakitic rocks.

In summary, the parental magmas that formed the fertile adakitic rocks in the study area were water rich, contained more mantle-derived material, and formed under more oxidizing magmatic conditions compared with the contemporaneous barren adakitic rocks in this region. The fact that Au and Cu are relatively enriched in the mantle (e.g., Richard, 2011) means that more oxidizing conditions would have prevented sulfide fractionation (e.g., Liang et al., 2006, 2009; Sun et al., 2013; Zou et al., 2015; Huang et al., 2017, 2018, 2019; Chen et al., 2019a,b). The high water contents of the magmas would also have enhanced volatile exsolution (e.g., Richards et al., 2012), making these magmas ideal for both the generation of Cu–Au enrichment and the subsequent formation of associated mineralization.

6.3. Two stages of Neo-Tethyan-related Cu–Au mineralization within the Gangdese belt

The southern Gangdese belt records the subduction of Neo-Tethyan oceanic crust during the Mesozoic and the subsequent collision of India with Eurasia during the Cenozoic (Chen, 2002; Chung et al., 2005; Ji et al., 2009a; Wen et al., 2008b; Zhu et al., 2011). Two magmatic suites associated with porphyry-type mineralization have been identified within the belt, including the Cenozoic post-collisional magmas that host porphyry Cu–Mo deposits within the south Gangdese porphyry belt (Hou et al., 2015a, 2015b; Qu et al., 2004) and Jurassic arc magmas that host the large porphyry-type Xiongcun Cu–Au deposit and a series of other mineralized occurrences (Chen et al., 2019a, b; Lang et al., 2014; Tafti et al., 2014; Tang et al., 2015; Zou et al., 2015, 2017). Previous research has identified an early Late Cretaceous magmatic 'flare-up' (ca. 100–80 Ma) within the southern Gangdese belt (Chung et al., 2005; Ji et al., 2009a; Ma et al., 2013a, 2013b, 2013c; Wen et al., 2008b; Zhu et al., 2011), but few mineral deposits in this region are associated with Cretaceous intrusions. Our new geochronological data indicate that the Kelu and Sangbujiala skarn-type Cu–Au deposits in the southeast Gangdese belt formed at ca. 93 Ma and ca. 95 Ma, respectively. These new ages indicate that the subduction of Neo-Tethyan oceanic crust formed two phases of Cu–Au mineralization within the south Gangdese belt, with these phases occurring during the Jurassic and the Cretaceous.

The large Jurassic Xiongcun porphyry-type Cu–Au deposit is thought to have formed as a result of Neo-Tethyan subduction (Lang et al., 2019; Wang et al., 2017). The early Late Cretaceous mafic and felsic rocks in regions close to the Kelu–Sangbujiala area (e.g., within the Zhengga and Milin areas) are thought to have formed as a result of rollback of the Neo-Tethyan slab (Ma et al., 2013a, 2013c). This suggests that the two stages of Cu–Au mineralization related to Neo-Tethyan subduction within the southern Gangdese belt formed as a result of Jurassic subduction (Fig. 12A) and Cretaceous slab rollback (Fig. 12B) events.

There are certainly fewer Cretaceous than Jurassic subduction-related Cu–Au deposits known in the southern Gangdese belt, but the reasons for this difference remain unclear. Previous research has suggested that barren Jurassic magmas were reduced and had lower $\varepsilon_{Nd}(t)$ and $\varepsilon_{Hf}(t)$ and higher $(^{87}Sr/^{86}Sr)_i$ ratios than those of the fertile Jurassic magmas in this area (Hou et al., 2015b; Wang et al., 2017), implying that contamination of magmas by reduced crustal material lessened the fertility of the barren magmas (Chen et al., 2019a,b). Both barren Late Cretaceous adakitic rocks and contemporaneous mafic rocks in this area have lower $\varepsilon_{Nd}(t)$ and higher $(^{87}Sr/^{86}Sr)_i$ ratios than those of the fertile adakitic rocks in the Kelu and Sangbujiala areas (Jiang et al., 2012; Ma et al., 2013a, 2013b, 2013c; Zhang et al., 2010; Zheng et al., 2014; Zhu et al., 2009) but have values that are similar to those of the barren Jurassic Yeba Formation (Fig. 9A). This suggests that the majority of the Cretaceous magmas in this area assimilated more crustal material than did the contemporaneous fertile magmas in this region. This addition of reduced crustal material might have made the magma less oxidized, preventing the magmas from becoming enriched in Cu and Au during their evolution (Chen et al., 2019a, 2019b; Deng and Wang, 2016). This can explain the lack of Cretaceous Cu–Au mineralization within the south Gangdese belt, although this also means that exploration for Cretaceous intrusion-related Cu–Au deposits in this region should focus on isotopically primitive intrusions with high whole-rock $\varepsilon_{Nd}(t)$ and low $(^{87}Sr/^{86}Sr)_i$ values.

7. Conclusions

1. The Kelu and Sangbujiala skarn Cu–Au deposits within the south Gangdese belt formed at ca. 92 Ma and ca. 95 Ma, respectively, and are both genetically related to Cretaceous intrusions.
2. The magmas that formed the Kelu and Sangbujiala deposits are adakitic and are likely to have formed as a result of partial melting of subducted Neo-Tethyan slab material, with the resulting magmas interacting with mantle peridotite material and fractionating amphibole prior to their emplacement.
3. The south Gangdese belt records two stages of Cu–Au mineralization related to the subduction of Neo-Tethyan oceanic crust.

Acknowledgments

This study was financially supported by the second Tibetan Plateau Scientific Expedition and Research (STEP; grant no. 2019QZKK0806) and the National Key R&D Program of China (grant no.

2016YFC0600407). This is contribution No.IS-2835 from GIGCAS.

Appendix A. Supplementary data

Supplementary data to this article can be found online at https://doi.org/10.1016/j.oregeorev.2020.103481.

References

Atherton, M.P., Petford, N., 1993. Generation of sodium-rich magmas from newly underplated basaltic crust. Nature 362 (6416), 144–146.

Ben Othman, D., White, W.M., Patchett, J., 1989. The geochemistry of marine sediments: island arc magma genesis and crust Cmantle recycling. Earth Planet. Sci. Lett. 94, 1–21.

Black, L.P., Kamo, S.L., Allen, C.M., Aleinikoff, J.N., Davis, D.W., Korsch, R.J., Foudoulis, C., 2003. TEMORA 1: a new zircon standard for Phanerozoic U-Pb geochronology. Chem. Geol. 200 (1–2), 155–170.

BGMRXAR (Bureau of Geology Mineral Resources of Xizang Autonomous Region), 1993, Regional Geology of Xizang (Tibet) Autonomus Region, Beijing, Geological Publishing House. pp.450.

Castillo, P.R., 2012. Adakite petrogenesis. Lithos v. 134, 304–316.

Castillo, P.R., Janney, P.E., Solidum, R.U., 1999. Petrology and geochemistry of Camiguin Island, southern Philippines: insights to the source of adakites and other lavas in a complex arc setting. Contrib. Miner. Petrol. 134 (1), 33–51.

Chauvel, C., Blichert-Toft, J., 2001. A hafnium isotope and trace element perspective on melting of the depleted mantle. Earth Planet. Sci. Lett. 190 (3–4), 137–151.

Chen, Y.J., 2002. Several important problems in study of regional metallogenesis in China: their relationship to continental collision: Earth. Sci. Front. 9 (2002), 319–328 (in Chinese with English abstract).

Chen, X.L., Richards, J.P., Liang, H.Y., Zou, Y.Q., Zhang, J., Huang, W.T., Ren, L., Wang, F.Y., 2019a. Contrasting arc magma fertilities in the Gangdese belt, Southern Tibet: evidence from geochemical variations of Jurassic volcanic rocks updates. Lithos 324, 789–802.

Chen, X.L., Liang, H.Y., Zhang, J., Sotiriou, P., Huang, W.T., Ren, L., Zhang, L., Zou, Y.Q., 2019b. Geochemical characteristics and magma fertility for the Jurassic arc rocks in the Gangdese belt, Tibet. Ore Geology Reviews v 115.

Chu, M.F., Chung, S.L., Song, B.A., Liu, D.Y., O'Reilly, S.Y., Pearson, N.J., Ji, J.Q., Wen, D.J., 2006. Zircon U-Pb and Hf isotope constraints on the Mesozoic tectonics and crustal evolution of southern Tibet. Geology 34 (9), 745–748.

Chung, S.L., Chu, M.F., Ji, J.Q., O'Reilly, S.Y., Pearson, N.J., Liu, D.Y., Lee, T.Y., Lo, C.H., 2009. The nature and timing of crustal thickening in Southern Tibet: Geochemical and zircon Hf isotopic constraints from postcollisional adakites. Tectonophysics 477 (1–2), 36–48.

Chung, S.L., Chu, M.F., Zhang, Y.Q., Xie, Y.W., Lo, C.H., Lee, T.Y., Lan, C.Y., Li, X.H., Zhang, Q., Wang, Y.Z., 2005. Tibetan tectonic evolution inferred from spatial and temporal variations in post-collisional magmatism. Earth Sci. Rev. 68 (3–4), 173–196.

Defant, M.J., Drummond, M.S., 1993. Mount-St-Helens - Potential Example of the Partial Melting of the Subducted Lithosphere in a Volcanic Arc. Geology 21 (6), 547–550.

Deng, J., Wang, Q., 2016. Gold mineralization in China: Metallogenic provinces, deposit types and tectonic framework. Gondwana Res. 36, 219–274.

Elburg, M.A., van Bergen, M., Hoogewerff, J., Foden, J., Vroon, P., Zulkarnain, I., Nasution, A., 2002. Geochemical trends across an arc-continent collision zone: magma sources and slab-wedge transfer processes below the Pantar Strait volcanoes, Indonesia. Geochim. Et. Cosmochim. Acta 66 (15), 2771–2789.

Guan, Q., Zhu, D.C., Zhao, Z.D., Dong, G.C., Zhang, L.L., Li, X.W., Liu, M., Mo, X.X., Liu, Y.S., Yuan, H.L., 2012. Crustal thickening prior to 38 Ma in southern Tibet: evidence from lower crust-derived adakitic magmatism in the Gangdese Batholith. Gondwana Res. 21 (1), 88–99.

Guo, Z.F., Hertogen, J., Liu, J.Q., Pasteels, P., Boven, A., Punzalan, L., He, H.Y., Luo, X.J., Zhang, W.H., 2005. Potassic magmatism in western Sichuan and Yunnan Provinces, SE Tibet, China: Petrological and geochemical constraints on petrogenesis. J. Petrol. 46 (1), 33–78.

Hou, Z.Q., Duan, L.F., Lu, Y.J., Zheng, Y.C., Zhu, D.C., Yang, Z.M., Yang, Z.S., Wang, B.D., Pei, Y.R., Zhao, Z.D., McCuaig, T.C., 2015a. Lithospheric architecture of the Lhasa Terrane and its control on ore deposits in the Himalayan-Tibetan Orogen. Econ. Geol. 110 (6), 1541–1575.

Hou, Z.Q., Qu, X.M., Wang, S.X., Du, A.D., Gao, Y.F., Huang, W., 2004. Re-Os age for molybdenite from the Gangdese porphyry copper belt on Tibetan plateau: implication for geodynamic setting and duration of the Cu mineralization. Sci. China Ser. D-Earth Sci. 47 (3), 221–231.

Hou, Z.Q., Yang, Z.M., Lu, Y.J., Kemp, A., Zheng, Y.C., Li, Q.Y., Tang, J.X., Yang, Z.S., Duan, L.F., 2015b. A genetic linkage between subduction- and collision-related porphyry Cu deposits in continental collision zones. Geology 43 (3), 247–250.

Hou, Z.Q., Yang, Z.M., Qu, X.M., Meng, X.J., Li, Z.Q., Beaudoin, G., Rui, Z.Y., Gao, Y.F., Zaw, K., 2009. The Miocene Gangdese porphyry copper belt generated during post-collisional extension in the Tibetan Orogen. Ore Geol. Rev. 36 (1–3), 25–51.

Huang, W., Liang, H.Y., Wu, J., Wang, C.L., Zou, Y.Q., Wang, X.Z., Xu, J.F., Charllote, M.T., 2013. Study on the metallogenesis during the early stage of continental collision in southern Gangdese, Tibet. Acta Petrol. Sin. v. 29 (4), 1439–1449.

Huang, W.T., Liang, H.Y., Wu, J., Zou, Y.Q., Zhang, J., 2017. Formation of porphyry Mo deposit in a deep fault zone, example from the Dabaoshan porphyry Mo deposit in northern Guangdong, South China. Ore Geol. Rev. 81, 940–952.

Huang, W.T., Liang, H.Y., Wu, L., Wu, J., Li, J., Bao, Z.W., 2018. Asynchronous formation of the adjacent epithermal Au-Cu and porphyry Cu-Mo deposits in the Zijinshan orefield, southeast China. Ore Geol. Rev. 102, 351–367.

Huang, W., Liang, H., Zhang, J., Wu, J., Chen, X., Ren, L., 2019. Genesis of the Dachang Sn-polymetallic and Baoshan Cu ore deposits, and formation of a Cretaceous Sn-Cu ore belt from southwest China to western Myanmar. Ore Geol. Rev. 112 103030.

Ingle, S., Weis, D., Doucet, S., Mattielli, N., 2003. Hf isotope constraints on mantle sources and shallow-level contaminants during Kerguelen hot spot activity since approximate to 120 Ma. Geochem. Geophys. Geosyst v. 4.

Ji, W.Q., Wu, F.Y., Chung, S.L., Li, J.X., Liu, C.Z., 2009a. Zircon U-Pb geochronology and Hf isotopic constraints on petrogenesis of the Gangdese batholith, southern Tibet. Chem. Geol. 262 (3–4), 229–245.

Ji, W.Q., Wu, F.Y., Liu, C.Z., Chung, S.L., 2009b. Geochronology and petrogenesis of granitic rocks in Gangdese batholith, southern Tibet. Sci. China Ser. D-Earth Sci. 52 (9), 1240–1261.

Jiang, Z.Q., Wang, Q., Li, Z.X., Wyman, D.A., Tang, G.J., Jia, X.H., Yang, Y.H., 2012. Late Cretaceous (ca. 90 Ma) adakitic intrusive rocks in the Kelu area, Gangdese Belt (southern Tibet): Slab melting and implications for Cu-Au mineralization. J. Asian Earth Sci. 53, 67–81.

Kang, Z.Q., Xu, J.F., Wilde, S.A., Feng, Z.H., Chen, J.L., Wang, B.D., Fu, W.C., Pan, H.B., 2014. Geochronology and geochemistry of the Sangri Group Volcanic Rocks, Southern Lhasa Terrane: Implications for the early subduction history of the Neo-Tethys and Gangdese Magmatic Arc. Lithos 200, 157–168.

Kay, R.W., Kay, S.M., 1993. Delamination and delamination magmatism. Tectonophysics 219 (1–3), 177–189.

Lang, X., Wang, X., Deng, Y., Tang, J., Xie, F., Zhou, Y., Huang, Y., Li, Z., Yin, Q., Jiang, K., 2019. Early Jurassic volcanic rocks in the Xiongcun district, southern Lhasa subterrane, Tibet: Implications for the tectono-magmatic events associated with the early evolution of the Neo-Tethys Ocean. Lithos v, 340–341.

Lang, X.H., Tang, J.X., Li, Z.J., Huang, Y., Ding, F., Yang, H.H., Xie, F.W., Zhang, L., Wang, Q., Zhou, Y., 2014. U-Pb and Re-Os geochronological evidence for the Jurassic porphyry metallogenic event of the Xiongcun district in the Gangdese porphyry copper belt, southern Tibet, PRC. J. Asian Earth Sci. 79, 608–622.

Li, J.W., Zhao, X.F., Zhou, M.F., Ma, C.Q., de Souza, Z.S., Vasconcelos, P., 2009. Late Mesozoic magmatism from the Daye region, eastern China: U-Pb ages, petrogenesis, and geodynamic implications. Contrib. Miner. Petrol. 157 (3), 383–409.

Li, J.X., Qin, K.Z., Li, G.M., Xiao, B., Chen, L., Zhao, J.X., 2011. Post-collisional ore-bearing adakitic porphyries from Gangdese porphyry copper belt, southern Tibet: melting of thickened juvenile arc lower crust. Lithos 126 (3–4), 265–277.

Li, X.H., Li, W.X., Li, Q.L., Wang, X.C., Liu, Y., Yang, Y.H., 2010. Petrogenesis and tectonic significance of the similar to 850 Ma Gangbian alkaline complex in South China: evidence from in situ zircon U-Pb dating, Hf-O isotopes and whole-rock geochemistry. Lithos 114 (1–2), 1–15.

Li, X.H., Qi, C.S., Liu, Y., Liang, X.R., Tu, X.L., Xie, L.W., Yang, Y.H., 2005. Petrogenesis of the Neoproterozoic bimodal volcanic rocks along the western margin of the YangtzeBlock: new constraints from Hf isotopes and Fe/Mn ratios. Chin. Sci. Bull. 50 (19), 109–114.

Li, X.H., Zhou, H.W., Chung, S.L., Lo, C.H., Wei, G.J., Liu, Y., Lee, C.Y., 2002. Geochemical and Sr-Nd isotopic characteristics of late paleogene ultrapotassic magmatism in southeastern Tibet. Int. Geol. Rev. 44 (6), 559–574.

Liang, H.-Y., Campbell, I.H., Allen, C., Sun, W.-D., Liu, C.-Q., Yu, H.-X., Xie, Y.-W., Zhang, Y.-Q., 2006. Zircon Ce4+/Ce3+ ratios and ages for Yulong ore-bearing porphyries in eastern Tibet. Miner. Deposita 41 (2), 152–159.

Liang, H.Y., Sun, W.D., Su, W.C., Zartman, R.E., 2009. Porphyry copper-gold mineralization at Yulong, China, promoted by decreasing redox potential during magnetite alteration. Econ. Geol. 104 (4), 587–596.

Liu, Y.S., Hu, Z.C., Zong, K.Q., Gao, C.G., Gao, S., Xu, J.A., Chen, H.H., 2010. Reappraisement and refinement of zircon U-Pb isotope and trace element analyses by LA-ICP-MS. Chin. Sci. Bull. 55 (15), 1535–1546.

Ludwig, K. R., 2003, User's manual for Isoplot 3.00: a geochronological toolkit for Microsoft Excel, Kenneth R. Ludwig, v. 4.

Ma, L., Wang, Q., Li, Z.X., Wyman, D.A., Jiang, Z.Q., Yang, J.H., Gou, G.N., Guo, H.F., 2013a. Early Late Cretaceous (ca. 93 Ma) norites and hornblendites in the Milin area, eastern Gangdese: Lithosphere-asthenosphere interaction during slab roll-back and an insight into early Late Cretaceous (ca. 100–80 Ma) magmatic "flare-up" in southern Lhasa (Tibet). Lithos 172, 17–30.

Ma, L., Wang, Q., Wyman, D.A., Jiang, Z.Q., Yang, J.H., Li, Q.L., Gou, G.N., Guo, H.F., 2013b. Late Cretaceous crustal growth in the Gangdese area, southern Tibet: Petrological and Sr-Nd-Hf-O isotopic evidence from Zhengga diorite-gabbro. Chem. Geol. 349, 54–70.

Ma, L., Wang, Q., Wyman, D.A., Li, Z.X., Jiang, Z.Q., Yang, J.H., Gou, G.N., Guo, H.F., 2013c. Late Cretaceous (100–89 Ma) magnesian charnockites with adakitic affinities in the Milin area, eastern Gangdese: Partial melting of subducted oceanic crust and implications for crustal growth in southern Tibet. Lithos v. 175, 315–332.

Macpherson, C.G., Dreher, S.T., Thirlwall, M.F., 2006. Adakites without slab melting: high pressure differentiation of island arc magma, Mindanao, the Philippines. Earth Planet. Sci. Lett. 243 (3–4), 581–593.

Mahoney, J.J., Frei, R., Tejada, M.L.G., Mo, X.X., Leat, P.T., Nagler, T.F., 1998. Tracing the Indian Ocean mantle domain through time: isotopic results from Old West Indian, East Tethyan, and South Pacific seafloor (vol 39, pg 1285, 1998). J. Petrol. 39 (11–12), 2153.

Martin, H., Moyen, J.F., 2002. Secular changes in tonalite-trondhjemite-granodiorite composition as markers of the progressive cooling of Earth. Geology 30 (4), 319–322.

Middlemost, E.A.K., 1994. Naming materials in the magma igneous rock system. Earth Sci. Rev. 37 (3–4), 215–224.

Nebel, O., Munker, C., Nebel-Jacobsen, Y.J., Kleine, T., Mezger, K., Mortimer, N., 2007.

Hf-Nd-Pb isotope evidence from Permian arc rocks for the long-term presence of the Indian-Pacific mantle boundary in the SW Pacific. Earth Planet. Sci. Lett. 254 (3–4), 377–392.
Pearce, N.J.G., Perkins, W.T., Westgate, J.A., Gorton, M.P., Jackson, S.E., Neal, C.R., Chenery, S.P., 1997. A compilation of new and published major and trace element data for NIST SRM 610 and NIST SRM 612 glass reference materials. Geostand. Newslett. J. Geostand. Geoanal. 21 (1), 115–144.
Peccerillo, A., Taylor, S.R., 1976. Geochemistry of eocene calc-alkaline volcanic-rocks from Kastamonu Area, Northern Turkey. Contribut. Mineral. Petrol. 58 (1), 63–81.
Plank, T., 2005. Constraints from thorium/lanthanum on sediment recycling at subduction zones and the evolution of the continents. J. Petrol. 46 (5), 921–944.
Qu, X.M., Hou, Z.Q., Li, Y.G., 2004. Melt components derived from a subducted slab in late orogenic ore-bearing porphyries in the Gangdese copper belt, southern Tibetan plateau. Lithos 74 (3–4), 131–148.
Rapp, R.P., Shimizu, N., Norman, M.D., Applegate, G.S., 1999. Reaction between slab-derived melts and peridotite in the mantle wedge: experimental constraints at 3.8 GPa. Chem. Geol. 160 (4), 335–356.
Rapp, R.P., Watson, E.B., 1995. Dehydration melting of metabasalt at 8–32-Kbar - implications for continental growth and Crust-Mantle recycling. J. Petrol. 36 (4), 891–931.
Richards, J.P., 2011. High Sr/Y arc magmas and porphyry Cu ± Mo ± Au deposits-Just add water. Econ. Geol. Bull. Soc. Econ. Geol. 107 (7), 1075–1581.
Richards, J.P., Spell, T., Rameh, E., Razique, A., Fletcher, T., 2012. High Sr/Y magmas reflect arc maturity, high magmatic water content, and porphyry Cu ± Mo ± Au potential: examples from the tethyan arcs of central and eastern iran and western Pakistan. Econ. Geol. 107 (2), 295–332.
Shimoda, G., Tatsumi, Y., Nohda, S., Ishizaka, K., Jahn, B.M., 1998. Setouchi high-Mg andesites revisited: geochemical evidence for melting of subducting sediments. Earth Planet Sci. Lett. 160 (3), 479–492.
Smoliar, M.I., Walker, R.J., Morgan, J.W., 1996. Re-Os ages of group IIA, IIIA, IVA, and IVB iron meteorites. Science 271 (5252), 1099–1102.
Streck, M.J., Leeman, W.P., Chesley, J., 2007. High-magnesian andesite from Mount Shasta: A product of magma mixing and contamination, not a primitive mantle melt. Geology 35 (1), 351–354.
Sun, S.S., McDonough, W.F., 1989. Chemical and isotopic systematics of oceanic basalt: implications for mantle compositions and processes. Geol. Soc. London Spec. Publicat. 42, 313–345.
Sun, W.D., Liang, H.Y., Ling, M.X., Zhan, M.Z., Ding, X., Zhang, H., Yang, X.Y., Li, Y.L., Ireland, T.R., Wei, Q.R., Fan, W.M., 2013. The link between reduced porphyry copper deposits and oxidized magmas. Geochim. Cosmochim. Acta 103, 263–275.
Sun, X.L., Li, M., Wang, G.X., Drosos, M., Liu, F.L., Hu, Z.Y., 2019. Response of phosphorus fractions to land-use change followed by long-term fertilization in a sub-alpine humid soil of Qinghai-Tibet plateau. J. Soils Sediments 19 (3), 1109–1119.
Sun, Y.L., Xu, P., Li, J., He, K., Chu, Z.Y., Wang, C.Y., 2010. A practical method for determination of molybdenite Re-Os age by inductively coupled plasma-mass spectrometry combined with Carius tube-HNO3 digestion. Anal. Methods 2 (5), 575–581.
Tafti, R., Lang, J.R., Mortensen, J.K., Oliver, J.L., Rebagliati, C.M., 2014. Geology and Geochronology of the Xietongmen (Xiongcun) Cu-Au Porphyry District, Southern Tibet, China. Econ. Geol. 109 (7), 1967–2001.
Tafti, R., Mortensen, J.K., Lang, J.R., Rebagliati, M., Oliver, J.L., 2009. Jurassic U-Pb and Re-Os ages for the newly discovered Xietongmen Cu-Au porphyry district, Tibet, PRC: implications for metallogenic epochs in the southern Gangdese belt. Econ. Geol. 104 (1), 127–136.
Tang, J.X., Lang, X.H., Xie, F.W., Gao, Y.M., Li, Z.J., Huang, Y., Ding, F., Yang, H.H., Zhang, L., Wang, Q., Zhou, Y., 2015. Geological characteristics and genesis of the Jurassic No I porphyry Cu-Au deposit in the Xiongcun district, Gangdese porphyry copper belt, Tibet. Ore Geol. Rev. 70, 438–456.
Tiepolo, M., Oberti, R., Zanetti, A., Vannucci, R., Foley, S.F., 2007. Trace-element partitioning between amphibole and silicate melt: Amphiboles. Cryst. Chem. Occurr. Health Issues 67, 417–451.
Tu, X.L., Zhang, H., Deng, W.F., Ling, M.X., Ying, L.H., Liu, Y., Sun, W.D., 2011. Application of resolution in-situ laser ablation ICP-MS in trace element analyses. Geochimica 40 (01), 83–98.
Vervoort, J.D., Patchett, P.J., 1996. Behavior of hafnium and neodymium isotopes in the crust: constraints from Precambrian crustally derived granites. Geochim. Et Cosmochim. Acta 60 (19), 3717–3733.
Vervoort, J.D., Patchett, P.J., Blichert-Toft, J., Albarede, F., 1999. Relationships between Lu-Hf and Sm-Nd isotopic systems in the global sedimentary system. Earth Planet. Sci. Lett. 168 (1–2), 79–99.
Wang, R., Richards, J.P., Hou, Z.Q., Yang, Z.M., Gu, Z.B., DuFrane, S.A., 2014a. Increasing Magmatic Oxidation State from Paleocene to Miocene in the Eastern Gangdese Belt, Tibet: implication for Collision-Related Porphyry Cu-Mo +/- Au Mineralization. Econ. Geol. 109 (7), 1943–1965.
Wang, R., Tafti, R., Hou, Z.Q., Shen, Z.C., Guo, N., Evans, N.J., Jeon, H., Li, Q.Y., Li, W.K., 2017. Across-arc geochemical variation in the Jurassic magmatic zone, Southern Tibet: implication for continental arc-related porphyry Cu-Au mineralization. Chem. Geol. 451, 116–134.
Wang, X.S., Bi, X.W., Chen, Y.W., Pan, L.C., Xu, L.L., 2019. Crystal fractionation of contaminated melts and re-melting of newly underplated basaltic crust generated Late Triassic andesitic and dioritic intrusions in the southern Yidun Terrane, SW China. Lithos 342, 135–151.
Wang, X.S., Bi, X.W., Leng, C.B., Zhong, H., Tang, H.F., Chen, Y.W., Yin, G.H., Huang, D.Z., Zhou, M.F., 2014b. Geochronology and geochemistry of Late Cretaceous igneous intrusions and Mo-Cu-(W) mineralization in the southern Yidun Arc, SW China: Implications for metallogenesis and geodynamic setting. Ore Geol. Rev. 61, 73–95.
Wei, G.J., Liang, X.R., Li, X.H., Liu, Y., 2002. Precisemeasurement of Sr isotopic composition of liquid and solid base using (LP) MC-ICPMS. Geochimica 31, 295–299.
Wen, D.R., Chung, S.L., Song, B., Iizuka, Y., Yang, H.J., Ji, J.Q., Liu, D.Y., Gallet, S., 2008a. Late Cretaceous Gangdese intrusions of adakitic geochemical characteristics, SE Tibet: Petrogenesis and tectonic implications. Lithos 105 (1–2), 1–11.
Wen, D.R., Liu, D.Y., Chung, S.L., Chu, M.F., Ji, J.Q., Zhang, Q., Song, B., Lee, T.Y., Yeh, M.W., Lo, C.H., 2008b. Zircon SHRIMP U-Pb ages of the Gangdese Batholith and implications for Neotethyan subduction in southern Tibet. Chem. Geol. 252 (3–4), 191–201.
Woodhead, J.D., Hergt, J.M., Davidson, J.P., Eggins, S.M., 2001. Hafnium isotope evidence for 'conservative' element mobility during subduction zone processes. Earth Planet. Sci. Lett. 192 (3), 331–346.
Wu, F.Y., Yang, Y.H., Xie, L.W., Yang, J.H., Xu, P., 2006. Hf isotopic compositions of the standard zircons and baddeleyites used in U–Pb geochronology. Chemical Geology 234, 105–126.
Xie, F.W., Tang, J.X., Chen, Y.C., Lang, X.H., 2018. Apatite and zircon geochemistry of Jurassic porphyries in the Xiongcun district, southern Gangdese porphyry copper belt: Implications for petrogenesis and mineralization. Ore Geol. Rev. 96, 98–114.
Xu, J.F., Castillo, P.R., 2004. Geochemical and Nd-Pb isotopic characteristics of the Tethyan asthenosphere: implications for the origin of the Indian Ocean mantle domain. Tectonophysics 393 (1–4), 9–27.
Xu, W.C., Zhang, H.F., Luo, B.J., Guo, L., Yang, H., 2015. Adakite-like geochemical signature produced by amphibole-dominated fractionation of arc magmas: an example from the Late Cretaceous magmatism in Gangdese belt, south Tibet. Lithos v. 232, 197–210.
Yin, A., Harrison, T.M., 2000. Geologic evolution of the Himalayan-Tibetan orogen. Annu. Rev. Earth Planet. Sci. 28, 211–280.
Zhang, L.L., Zhu, D.C., Wang, Q., Zhao, Z.D., Liu, D., Xie, J.C., 2019. Late Cretaceous volcanic rocks in the Sangri area, southern Lhasa Terrane, Tibet: evidence for oceanic ridge subduction. Lithos v. 326, 144–157.
Zhang, S.Q., Mahoney, J.J., Mo, X.X., Ghazi, A.M., Milani, L., Crawford, A.J., Guo, T.Y., Zhao, Z.D., 2005. Evidence for a widespread Tethyan upper mantle with Indian-Ocean-type isotopic characteristics. J. Petrol. 46 (4), 829–858.
Zhang, Z., Zhao, G., Santosh, M., Wang, J., Dong, X., Shen, K., 2010. Late Cretaceous charnockite with adakitic affinities from the Gangdese batholith, southeastern Tibet: Evidence for Neo-Tethyan mid-ocean ridge subduction? Gondwana Res. 17 (4), 615–631.
Zheng, Y.C., Hou, Z.Q., Gong, Y.L., Liang, W., Sun, Q.Z., Zhang, S., Fu, Q., Huang, K.X., Li, Q.Y., Li, W., 2014. Petrogenesis of Cretaceous adakite-like intrusions of the Gangdese Plutonic Belt, southern Tibet: Implications for mid-ocean ridge subduction and crustal growth. Lithos v. 190, 240–263.
Zhu, D.C., Wang, Q., Cawood, P.A., Zhao, Z.D., Mo, X.X., 2017. Raising the Gangdese Mountains in southern Tibet. J. Geophys. Res. -Solid Earth 122 (1), 214–223.
Zhu, D.C., Zhao, Z.D., Niu, Y.L., Mo, X.X., Chung, S.L., Hou, Z.Q., Wang, L.Q., Wu, F.Y., 2011. The Lhasa Terrane: record of a microcontinent and its histories of drift and growth. Earth Planet. Sci. Lett. 301 (1–2), 241–255.
Zhu, D.C., Zhao, Z.D., Pan, G.T., Lee, H.Y., Kang, Z.Q., Liao, Z.L., Wang, L.Q., Li, G.M., Dong, G.C., Liu, B., 2009. Early cretaceous subduction-related adakite-like rocks of the Gangdese Belt, southern Tibet: products of slab melting and subsequent melt-peridotite interaction? J. Asian Earth Sci. 34 (3), 298–309.
Zou, Y.Q., Chen, X.L., Huang, W.T., Zhang, J., Liang, H.Y., Xu, J.F., Chen, L., 2017. Identification of an Early-Middle Jurassic oxidized magmatic belt, south Gangdese, Tibet, and geological implications. Sci. Bull. 62 (12), 888–898.
Zou, Y.Q., Huang, W.T., Liang, H.Y., Wu, J., Lin, S.P., Wang, X.Z., 2015. Identification of porphyry genetically associated with mineralization and its zircon U-Pb and biotite Ar-Ar age of the Xiongcun Cu-Au deposit, southern Gangdese, Tibet. Acta Petrol. Sin. 31 (7), 2053–2062.